

Type II radio bursts:

1. New entirely analytic formalism for the electron beams, Langmuir waves, and radio emission

J. M. Schmidt¹ and Iver H. Cairns¹

Received 31 October 2011; revised 17 January 2012; accepted 3 March 2012; published 21 April 2012.

[1] Type II radio bursts drift in frequency as shock waves and coronal mass ejections (CMEs) move through the Sun's corona and the solar wind. This paper extends the theoretical models for type II radio bursts of Knock et al. (2001, 2003), Knock and Cairns (2005), Cairns and Knock (2006) and Schmidt and Gopalswamy (2008). The theory treats the acceleration of electrons at the shock, formation of electron beams, growth of Langmuir waves, and conversion of Langmuir energy into radiation. An entirely analytical and more general formalism is developed, which includes kappa electron velocity distribution functions for the plasma electrons and the shock-reflected electron beam. The radiation model also includes the plateauing of the electron beam, which releases energy for the Langmuir waves. This paper has two parts. First, the new entirely analytical formalism is presented. Second, first numerical results for synthetic radio images and synthetic dynamic spectra are discussed, gained by applying our radiation model to MHD simulations of a shock driven by a CME. The results are compared with earlier analytic approaches. This work is also applicable to other shock-related emissions in space and astrophysical plasmas.

Citation: Schmidt, J. M., and I. H. Cairns (2012), Type II radio bursts: 1. New entirely analytic formalism for the electron beams, Langmuir waves, and radio emission, *J. Geophys. Res.*, 117, A04106, doi:10.1029/2011JA017318.

1. Introduction

[2] Propagating shock waves in the solar corona and interplanetary medium have long been associated with type II solar radio emission [Wild and Smerd, 1972; Cane et al., 1981; Nelson and Melrose, 1985; Lengyel-Frey et al., 1997; Mann and Klassen, 2005]. Strong associations between type IIs and the shocks ahead of coronal mass ejections (CMEs) have been shown in recent observations, particularly in the interplanetary medium. While CMEs can drive shock waves via a piston mechanism in a plasma [see, e.g., Temmer et al., 2009], very fast coronal shocks may also be blast waves ignited by the pressure pulse of a flare [see, e.g., Nindos et al., 2011]. There is strong evidence that at least some type IIs are generated in electron foreshock regions upstream of the shock waves ahead of CMEs [Cane et al., 1981; Reiner et al., 1997, 1998; Bale et al., 1999; Reiner and Kaiser, 1999; Pulupa et al., 2010; Cairns, 2011]. These observations have demonstrated that (1) the emission is consistent with generation near the upstream electron plasma frequency f_p and near $2f_p$, (2) the source regions travel away from the Sun at speeds of hundreds of km s^{-1} , as indicated in plots of the inverse

emission frequency versus time [see, e.g., Reiner, 2000], consistent with a propagating shock, and (3) Langmuir waves and electron beams occur in the foreshock region ahead of an active type II-emitting CME-driven shock.

[3] CMEs carry away mass and momentum from the corona of the Sun and are widely recognized as major transient events [e.g., Hundhausen, 1999]. Their speeds lie in the range 100 km s^{-1} to 3000 km s^{-1} or more, with masses as large as 10^{13} kg [Hundhausen, 1999; St. Cyr et al., 2000; Gopalswamy, 2006]. Coronagraphs such as the Large Angle Spectrometric Coronagraph (LASCO) [Hundhausen et al., 1984; Brueckner et al., 1995] on the Solar and Heliospheric Observatory (SoHO), the Sun Earth Connection Coronal and Heliospheric Investigation instrument (SECCHI) [Howard et al., 2008] on the Solar TERrestrial Relations Observatory (STEREO), and the Atmospheric Imaging Assembly instrument (AIA) [Lemen et al., 2011] on the Solar Dynamics Observatory (SDO) are imaging CMEs. They can also be observed as interplanetary CMEs (ICMEs) by spacecraft in situ [e.g., Klein and Burlaga, 1982; Sheeley et al., 1985; Crooker et al., 1997]. CMEs moving faster than the local fast mode speed can drive shocks, which in turn accelerate electrons that produce type II radio bursts [see, e.g., Cane and Stone, 1984]. These form typically from a heliocentric distance $< 2R_{\odot}$ on [e.g., Gopalswamy et al., 2005], where CME observations are hard to obtain. Moreover, fast CMEs traverse the inner corona quickly, leaving few captured details in low cadence images. Thus, a precise prediction of the

¹School of Physics, University of Sydney, Sydney, New South Wales, Australia.

behavior of CMEs for space weather applications requires a proper knowledge of their properties below $\sim 4R_{\odot}$ heliocentric distance [see, e.g., *Gopalswamy et al.*, 2000] and fast cadence observations from SDO and STEREO.

[4] The standard interpretation of metric and kilometric type II radio bursts is that they are caused by shock-accelerated electrons that generate radiation at the local upstream plasma frequency and its second harmonic [*Wild and Smerd*, 1972; *Nelson and Melrose*, 1985; *Cairns*, 2011]. An association between interplanetary (hectometric and kilometric) type II bursts and CME driven shocks is firmly established, with type II radio emission generated upstream of the CME-driven shock [*Cane et al.*, 1987; *Reiner et al.*, 1998; *Bale et al.*, 1999]. An example of a type II radio tracking facility is the radio receiver RAD2 of the WAVES experiment on board the Wind spacecraft, measuring between 1.075 MHz and 13.825 MHz [e.g., *Bougeret et al.*, 1995], which avoids the ionospheric cutoff at Earth for radio signals below 10 MHz originating above about 2–3 R_{\odot} heliocentric distance. Closer to the Sun, radio observations can be made by ground-based radio instruments, e.g., the Nançay radioheliograph, imaging at five discrete frequencies between 164 MHz and 432 MHz. Radio type II bursts with a “herringbone” fine structure have been measured and investigated for many years for instance with the radio spectralpolarimeter of the Astrophysical Institute Potsdam (Germany) within the range 40–800 MHz [*Nelson and Melrose*, 1985; *Mann and Klassen*, 2005, and references therein]. A sharpening of the images can be obtained by correlating spatially distributed antennas, as done with the LOw Frequency ARray (LOFAR) that covers plasma frequencies at distances between approximately 1.3 and 2.3 R_{\odot} from the Sun’s center [*Röttgering et al.*, 2005], or the Murchison Widefield Array (MWA) for frequencies between 80 and 300 MHz with an equivalent field of view [*Salah et al.*, 2005].

[5] Four main steps are involved in the accepted picture for type II emission [e.g., *Nelson and Melrose*, 1985; *Cairns*, 2011]: (1) acceleration of electrons at or near the shock; (2) accelerated electrons form beam distributions in velocity space in the foreshock region; (3) beam distributions are unstable to the generation of Langmuir waves via wave particle interactions; and (4) some Langmuir energy is coupled into electromagnetic emission, leading to the observed type II burst. *Holman and Pesses* [1983], *Nelson and Melrose* [1985], *Cairns* [1986a], and *Benz and Golla* [1988] have considered qualitative models for type II production in foreshock regions upstream of shocks.

[6] Literature dealing with acceleration processes at fast mode MHD shocks includes that by *Sonnerup* [1969], *Toptyghin* [1980], *Potter* [1981], *Holman and Pesses* [1983], *Webb et al.* [1983], *Goodrich and Scudder* [1984], *Leroy and Mangeney* [1984], *Wu* [1984], and *Yuan et al.* [2007]. These works treat electron and ion acceleration for both reflected and transmitted particles. It is thought that the type II emission region lies upstream of the shocks [*Cane et al.*, 1981; *Cairns*, 1986a; *Lengyel-Frey et al.*, 1997; *Reiner et al.*, 1998; *Bale et al.*, 1999]. Thus, the reflection process is of primary concern.

[7] For the decision what electron acceleration process is relevant, the angle θ_{bn} between the upstream magnetic field direction and the local shock normal is an important

quantity. In the case that the gyroradii of the particles are large compared with the shock ramp, the acceleration of reflected electrons by the moving magnetic mirror of quasi-perpendicular shocks ($|\theta_{bn}| \geq 45^\circ$) is sometimes called shock drift acceleration (SDA) [*Toptyghin*, 1980]. When the gyroradii are smaller, the reflection is sometimes called magnetic mirror reflection instead [*Wu*, 1984]. The energy comes from net gradient and/or curvature drift parallel to the sign of the charge times the convection electric field. The process produces large relative energy gains when $|\theta_{bn}| \sim 90^\circ$.

[8] The occasional connection of an upstream spacecraft to two magnetic tangent points ($\theta_{bn} = 90^\circ$) on opposite sides of the spacecraft prior to the shock crossing (with $\theta_{bn} \sim 86^\circ$ at the crossing) is suggested by *Bale et al.*’s [1999] in situ observation of a shock associated with an interplanetary type II. These observations imply ripples of the shock surface [*Bale et al.*, 1999; *Knock et al.*, 2003b; *Neugebauer and Giacalone*, 2005; *Knock and Cairns*, 2005; *Pulupa et al.*, 2010]. In that case, parts of the shock magnetically connected to the upstream region need not have the same θ_{bn} as at the shock crossing. The same is likely if the shock is curved (even without ripples) or if \mathbf{B} varies in space. In such a situation one would expect an upstream region connected to a whole range of θ_{bn} , where one or more points with $|\theta_{bn}| \sim 90^\circ$ are present.

[9] Much work has been carried out on the growth of electron beam-driven Langmuir waves in plasmas [e.g., *Filbert and Kellogg*, 1979; *Melrose*, 1985; *Lacombe et al.*, 1988; *Cairns and Fung*, 1988]. In particular, a stochastic growth theory (SGT) of plasma waves has been developed that can successfully explain the Langmuir waves driven by electron beams producing type III solar radio bursts [*Robinson*, 1992; *Robinson et al.*, 1993a; *Robinson and Cairns*, 1998b; *Robinson and Benz*, 2000], thermal waves in the solar wind [*Cairns et al.*, 2000], and Langmuir waves driven by electron beams in Earth’s foreshock [*Cairns and Robinson*, 1997, 1999; *Cairns et al.*, 2000]. Thus, SGT can be considered a natural candidate theory for the Langmuir waves involved in type II foreshock emission.

[10] *Holman and Pesses* [1983], *Cairns* [1986a], *Benz and Golla* [1988], and *Street et al.* [1994] attempted to produce models of type II solar radio bursts, previously, which are based on the same primary acceleration mechanism. However, neither calculations of beam distributions throughout the foreshock, nor studies of the resulting Langmuir waves and radio emission processes were included in their work. *Fitzenreiter et al.* [1990] calculated foreshock beams at a curved shock analytically. *Knock et al.* [2001] calculated foreshock beams, applied SGT, and calculated the radio emission of type II solar radio bursts for the first time. Their work included a detailed model for electron reflection and beam production and was applied to the type II shock geometry estimated from the observations by *Bale et al.* [1999]. The Langmuir wave growth was modeled using SGT and the conversion of Langmuir wave energy into freely propagating radio emission using specific nonlinear three-wave processes. This approach allowed calculation of the radiation flux at a distant observer for comparison with observations.

[11] The influence of shock ripples on the dynamical spectra was further discussed by *Knock et al.* [2003b], and shown to produce significant fine structures in time and

frequency. *Knock and Cairns* [2005] and *Cairns and Knock* [2006] included the modeling of coronal and interplanetary structures. A further improvement of the model was achieved by including a data-driven model for the solar wind with both radial and longitudinal (azimuthal) variations in plasma parameters, again leading to significant fine structures and variability of the dynamic spectrum [*Florens et al.*, 2007]. *Hillan et al.* [2011] carried out a first detailed comparison of this model with observations.

[12] *Schmidt and Gopalswamy* [2008] replaced the computing-intensive numerical evaluations of phase space integrals for the calculation of reflected beam parameters in the type II theory [*Knock et al.*, 2001, 2003a, 2003b; *Knock and Cairns*, 2005; *Cairns and Knock*, 2006; *Florens et al.*, 2007] with analytic results of these beam parameters for Maxwellian electron velocity distributions in the solar wind, and combined the then completely analytical radiation theory with MHD simulations of a CME-driven shock. They were able to simulate the radio map observations of *Maia et al.* [2000]. A number of limitations exist for that calculation and for previous theories for type II bursts [*Cairns*, 2011].

[13] In the study presented here we revise and extend the work of *Knock et al.* [2001, 2003a, 2003b], *Knock and Cairns* [2005], *Cairns and Knock* [2006], and *Schmidt and Gopalswamy* [2008] related to radio emission at CME-driven shocks, extending the foregoing theory with analytic results for the reflection efficiency, intrinsic electron beam distribution functions, and plateaued electron distributions, which result from an erosion of that reflected distribution as Langmuir waves are generated, for kappa velocity distributions of electrons in the background solar wind plasma. Note that kappa distributions have elongated high velocity tails that better suit solar wind conditions [see, e.g., *Maksimovic et al.*, 1997]. Our analytic results yield a kinetic theory for radio emission that can be combined with or bolted onto MHD simulations of CMEs driving shock waves or to other shock simulations (MHD or otherwise) in different coronal or astrophysical systems. Our new calculations correct the work of *Schmidt and Gopalswamy* [2008] to remove downstream emission, extend the emission theory of *Knock* and collaborators to be fully analytic and to fully include kappa electron distribution functions for the typically nonthermal solar wind electrons, and also show how to better capture the front of the shock in the MHD simulation. In particular, there is no emission arising from the downstream region any longer, which appeared in the previous bolt-on calculations.

[14] The work presented here uses this new “bolt-on” theory to predict the radio emission produced upstream of the nose (most anti-sunward region) of a CME-driven shock. The shock is predicted using an MHD simulation code. We obtain a much more refined picture of shock radiation than in the work by *Schmidt and Gopalswamy* [2008]. A full description of the radio results, including radiation from the flanks of the expanding CME-driven shock is given in the companion paper (Schmidt, J. M., and I. H. Cairns, Type II radio bursts: 2. Applications of new analytic formalism, manuscript in preparation for *Journal of Geophysical Research*, 2012, hereinafter referred to as Schmidt and Cairns, manuscript in preparation, 2012). The new “bolt-on” theory should be applicable to other phenomena like a CME interacting with a corotating interaction region, erupting loops in the

corona responsible for decimetric radio bursts, or reconnection-driven beams.

[15] This paper is structured as follows. In section 2 we present our new reflection results based on kappa electron distributions. Section 3 presents our analytic results for the plateauing effect and the plateaued electron distributions used to predict the energy flow into the Langmuir waves. In section 4 we summarize the analytic description of the Langmuir growth and the production of electromagnetic radiation, while section 5 introduces our MHD model for shock excitation. How we identify the shock in the MHD simulation is explained in section 6. Section 7 presents and discusses our initial results for simulated radio maps and dynamic spectra. Section 8 ends with the conclusions and summary.

2. Reflection Results

[16] Figure 1 shows the definitions of the shock parameters used. The shock front can be seen as the thick line, which is a location for an entropy jump and a steep increase of the plasma density and magnetic field strength in the MHD simulations. The vectors \mathbf{n} and \mathbf{t} are unit vectors normal and tangential to a distinctive point on the shock front. The shock itself has a velocity in the normal direction. A velocity component in the tangential direction is possible too, when the local shock is on the flank region of a ballistically moving CME. The region of the plasma into which the shock is moving is the upstream region. Specifically, the direction “upstream” means “directed upstream away from the shock”. The region behind the shock’s magnetic mirror is the downstream region. The vector \mathbf{u} denotes the velocity of the plasma relative to the shock, and \mathbf{B} is the magnetic field vector that intersects the shock at a specific point. The angle θ_{bu} is between \mathbf{u} and \mathbf{B} , and the angle θ_{bn} is the angle between \mathbf{B} and the shock normal \mathbf{n} .

[17] For this geometry, assuming a Maxwellian velocity distribution for solar wind electrons moving into the shock, *Knock et al.* [2001] derived the reduced (integrated over perpendicular velocity) electron distribution function reflected at the shock front

$$F_r(v_{\parallel r}) = \eta(v_{\parallel})F(v_{\parallel}), \quad (1)$$

where $\eta(v_{\parallel})$ is the reflection efficiency, $F(v_{\parallel})$ the reduced distribution function of incident electrons with speed v_{\parallel} parallel to the magnetic field,

$$v_{\parallel r} = -v_{\parallel} - 2v_{\parallel}^{WH} + u \cos \theta_{bu}, \quad (2)$$

is the (parallel) velocity component of a reflected electron in the direction of the magnetic field, $v_{\parallel}^{WH} = -v_d \tan \theta_{bn}$ is the parallel component of the relative velocity between the solar wind frame and the de Hoffmann-Teller rest frame of the shock, where $v_d = |-(\mathbf{u} \times \mathbf{B}) \times \mathbf{B}/B^2|$ is the bulk drift velocity of the upstream plasma perpendicular to the magnetic field \mathbf{B} (and the convection electric field $\mathbf{E} = -\mathbf{u} \times \mathbf{B}$), and $u \cos \theta_{bu}$ is the bulk speed of the upstream plasma parallel to the magnetic field. The quantity $v_c = v_d \tan \theta_{bn} = v_{\parallel}^{WH}$ is also called the cutoff speed for shock reflection [*Cairns*, 1987a], since any reflected electron that escapes upstream of the shock must have been accelerated to at least the

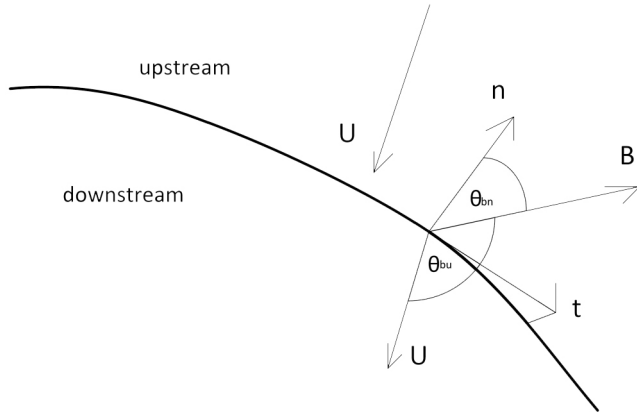


Figure 1. Definitions of the shock parameters. The thick line represents the shock surface.

speed v_c with which the shock moves along $\pm \mathbf{B}$ through the solar wind.

[18] Equations (1) and (2) are based upon conservation of the magnetic moment and energy in the shock's de Hoffman-Teller frame, in which the convection electric field vanishes on both sides of the shock. Reviews of the physics exist elsewhere [e.g., *Wu, 1984; Cairns, 2011*] and only final results are given here. Equation (2) expresses momentum conservation of electrons reflected at the shock's magnetic mirror in the Hoffman-Teller frame. The reflection efficiency at the shock is defined as

$$\eta(v_{\parallel}) = \frac{\int_0^{v_c} 2\pi v_{\perp} f(v_{\parallel}, v_{\perp}) dv_{\perp}}{\int_0^c 2\pi v_{\perp} f(v_{\parallel}, v_{\perp}) dv_{\perp}}, \quad (3)$$

where c is the speed of light and $f(v_{\parallel}, v_{\perp})$ is the electron velocity distribution incident on the shock. The shock's magnetic jump and the cross-shock electrostatic potential define a loss-cone for electrons reflected from the shock, as shown in Figure 2. The quantity v_{lc} is the minimum perpendicular speed of the loss cone for reflected electrons with speed v_{\parallel} . The conservation of magnetic moment and energy in the de Hoffman-Teller frame imply that

$$v_{lc}^2 = \frac{(v_{\parallel} - v_d \tan \theta_{bn})^2 + \frac{2}{m_e} e \Delta \Phi'}{B_2/B_1 - 1}, \quad (4)$$

where v_{\parallel} is taken in the shock's rest frame. Here, $e \Delta \Phi'$ is an electrostatic cross-shock potential, which contributes to the electron acceleration, and B_2 and B_1 are the magnetic field strengths downstream and upstream of the shock, respectively. Ideally, B_2 and $\Delta \Phi'$ are the overshoot values. As usual e and m_e are the electron charge and mass, respectively. Thus $\eta(v_{\parallel})$ is the ratio of the number of electrons incident on the shock with speed v_{\parallel} that are outside the loss cone (defined by the macroscopic electric and magnetic fields) with v_{\perp} between v_{lc} and c , and the total number of electrons incident on the shock with speed v_{\parallel} . Note that if the minimum perpendicular speed of the loss-cone v_{lc} for

a given v_{\parallel} in the reflection process becomes larger, then a smaller number of electrons is reflected, and the reflection efficiency becomes smaller.

[19] Figure 2, taken from *Yuan et al. [2008]*, shows the electron velocity distribution upstream of a quasi-perpendicular shock with $\theta_{bn} = 85^\circ$, obtained by following test particle electrons through the \mathbf{E} and \mathbf{B} fields predicted by a 1 D hybrid simulation. The Maxwellian electron velocity distribution incident on the shock is the distribution on the positive v_{\parallel} axis in this figure. The dotted line is the ideal loss cone for the reflected electrons (negative v_{\parallel}) when only magnetic effects are included, and the dash-dotted line is the actual loss cone for the same shock when the electrostatic cross shock potential is included, which is distorted to a hyperboloid. We can see clearly that the reflected electrons occur at v_{\perp} values above the hyperbolic line along the negative v_{\parallel} axis. The small population of electrons between the hyperbolic line and the v_{\parallel} axis are due to leakage of electrons from the downstream region. The quantity v_{lc} is the value of v_{\perp} on the loss cone for a given v_{\parallel} value.

[20] Using conservation of magnetic moment and energy, and isotropic Maxwellian electron velocity distribution functions, it can be shown [*Knock et al., 2001*] that

$$\eta(v_{\parallel}) = 1 - \operatorname{erf} \left[\frac{v_{lc}}{v_e \sqrt{2}} \right] + \frac{v_{lc} e^{-v_{lc}^2/2v_e^2}}{v_e \sqrt{\pi/2}}. \quad (5)$$

Here, the error function $\operatorname{erf}(x) = (2/\sqrt{\pi}) \int_0^x e^{-t^2} dt$. This

reflection efficiency depends on the thermal electron speed $v_e = (k_B T_e / m_e)^{1/2}$, where k_B is Boltzmann's constant and T_e is the electron temperature.

[21] The number density n_b of the reflected electron beam, the mean parallel velocity v_b of the reflected electrons (e.g., the beam speed), and the standard deviation Δv_b of the parallel velocities of the reflected electrons from the mean value are given by the moments

$$n_b = \int_{v_c}^{\infty} F_r(v_{\parallel r}) dv_{\parallel r}, \quad (6)$$

$$v_b = \int_{v_c}^{\infty} v_{\parallel r} F_r(v_{\parallel r}) dv_{\parallel r}, \quad (7)$$

$$\langle v_{\parallel r}^2 \rangle = \int_{v_c}^{\infty} v_{\parallel r}^2 F_r(v_{\parallel r}) dv_{\parallel r}, \quad (8)$$

$$\Delta v_b = \sqrt{\langle v_{\parallel r}^2 \rangle - v_b^2}. \quad (9)$$

Note that in the plasma rest frame the parallel speeds of the reflected electrons range from v_c to c (approximated by ∞ here), which defines the limits of these moment integrals. *Schmidt and Gopalswamy [2008]* evaluated (6), (7), and (9) analytically for a $F_r(v_{\parallel r})$ that is a product of a Maxwellian with the reflection efficiency (5).

[22] Now, we discuss our new analytic approach to the reflection process using kappa electron velocity distribution functions. Following for example *Knock et al. [2003a]*,

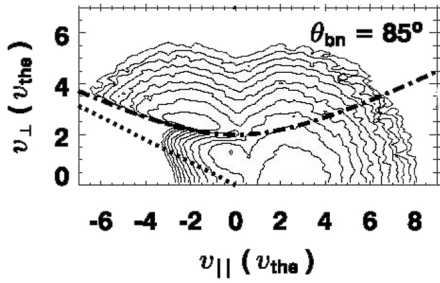


Figure 2. Simulated electron velocity distribution in the shock normal frame upstream of a shock with $\theta_{bn} = 85^\circ$, Alfvén Mach number $M_A = 7.7$, and sonic Mach number $M_s = 5.0$, taken from *Yuan et al.* [2008]. Dash-dotted and dotted lines show the loss cones defined by the shock’s magnetic mirror with and without, respectively, the cross-shock potential. Reflected electrons occur at $v_{\parallel} < 0$ and downgoing electrons at $v_{\parallel} > 0$. Here $v_{the} = v_e$ is the upstream electron thermal speed.

electrons can be modeled with normalized kappa velocity distribution functions

$$f_{\kappa}(v_{\parallel}, v_{\perp}) = \frac{\Gamma(\kappa + 1)}{\Gamma(\kappa - \frac{1}{2})} \pi^{-3/2} v_e^{-3} \left(1 + \frac{v_{\parallel}^2 + v_{\perp}^2}{v_e^2}\right)^{-(\kappa+1)}, \quad (10)$$

where v_{\parallel} and v_{\perp} are the velocity components parallel and perpendicular to the magnetic field. These distribution functions have enhanced high velocity tails extending to ∞ , whose height or strength depends on κ . They are known to describe well electron distributions observed in the solar wind [see, e.g., *Maksimovic et al.*, 1997], and reasonable values are $2 \leq \kappa \leq 5$. A detailed derivation (Appendix A) leads to the reduced distribution function outside the loss cone,

$$F_{loss-cone} = \int_{v_c}^{\infty} 2\pi v_{\perp} f_{\kappa}(v_{\parallel}, v_{\perp}) dv_{\perp} \quad (11)$$

$$\approx \frac{\Gamma(\kappa + 1)}{\Gamma(\kappa - \frac{1}{2})} \pi^{-1/2} \frac{v_e^{-1}}{\kappa} \left(1 + \frac{v_{\parallel}^2 + v_c^2}{v_e^2}\right)^{-\kappa}. \quad (12)$$

Equivalently, we obtain the incident reduced electron distribution

$$F_i(v_{\parallel}) = \int_0^{\infty} 2\pi v_{\perp} f_{\kappa}(v_{\parallel}, v_{\perp}) dv_{\perp} \quad (13)$$

$$\approx \frac{\Gamma(\kappa + 1)}{\Gamma(\kappa - \frac{1}{2})} \pi^{-1/2} \frac{v_e^{-1}}{\kappa} \left(1 + \frac{v_{\parallel}^2}{v_e^2}\right)^{-\kappa}, \quad (14)$$

moving toward the shock from upstream. Thus, the reflection efficiency can be expressed as:

$$\eta(v_{\parallel}) \approx \left(\frac{v_e^2 + v_{\parallel}^2 + v_c^2}{v_e^2 + v_{\parallel}^2}\right)^{-\kappa} \quad (15)$$

for kappa electron distribution functions. Since the reflected electron distribution $F_r(v_{\parallel})$ is the reflection efficiency times the velocity distribution incident on the shock, we find

$$F_r(v_{\parallel}) \approx \frac{\Gamma(\kappa + 1)}{\Gamma(\kappa - \frac{1}{2})} \pi^{-1/2} \frac{v_e^{-1}}{\kappa} \left(1 + \frac{v_{\parallel}^2 + v_c^2}{v_e^2}\right)^{-\kappa}, \quad (16)$$

where v_c^2 is the function in (4). Thus far the analysis is for electrons in the de Hoffman-Teller frame. Now (16) is applied to a population of reflected beam electrons in the shock frame in which v_{\parallel} ranges from $v_c = v_d \tan \theta_{bn}$ to infinity, since electrons are accelerated to at least the cutoff speed v_c by reflection. Outside this range $F_r(v_{\parallel})$ is zero for this population. We can consider this property by multiplying (16) with a Heaviside step-function $H(v_{\parallel}, v_c)$, which is zero for $v_{\parallel} < v_c$ and one for $v_{\parallel} \geq v_c$:

$$F_r(v_{\parallel}) \approx \frac{\Gamma(\kappa + 1)}{\Gamma(\kappa - \frac{1}{2})} \pi^{-1/2} \frac{v_e^{-1}}{\kappa} \left(1 + \frac{v_{\parallel}^2 + v_c^2}{v_e^2}\right)^{-\kappa} H(v_{\parallel}, v_c). \quad (17)$$

[23] Figure 3 shows the reflection efficiencies in the de Hoffman-Teller frame: $\eta_M(v_{\parallel})$ (dotted line) according to the original *Knock et al.* [2001] and *Schmidt and Gopalswamy* [2008] approach, using Maxwellian distributions and given by (5), and $\eta_K(v_{\parallel})$ (solid line) according to the new approach, using kappa distribution functions and given by (15). Parameters used in Figure 3 and in the simulation in sections 5–7 are $T_e = 3 \times 10^4$ K, $B_1 = 4$ nT, $B_2 = 8$ nT, $v_d = 700$ km s $^{-1}$, and $\theta_{bn} = 45^\circ$, resulting in $v_e = 674$ km s $^{-1}$, and $v_c = 700$ km s $^{-1}$. We have chosen $\kappa = 2.5$, which is a typical value for the solar wind based on an extensive study of ULYSSES electron measurements [see, e.g., *Maksimovic et al.*, 1997]. Furthermore, we used the approximation $e\Delta\Phi' \approx 2k_B T_e (B_2/B_1 - 1)$ from *Kuncic et al.* [2002].

[24] We see that $\eta_M(v_{\parallel})$ is a slightly distorted Maxwellian that has a maximum of about 0.26 at $v_{\parallel} \approx 7.0 \times 10^5$ m s $^{-1}$, rapidly decreases for larger v_{\parallel} , and is smaller than 0.01 for $v_{\parallel} \geq 2.6 \times 10^6$ m s $^{-1}$. This means that in the Maxwellian theory electrons are reflected best when $v_{\parallel} \approx v_e$, but reflection of faster electrons is rare.

[25] In contrast, $\eta_K(v_{\parallel})$ starts with about 0.01 at $v_{\parallel} = 0$, which is much smaller than $\eta_M(0) \approx 0.17$, and increases to a maximum of about 0.25 at about $v_{\parallel} = 3 \times 10^6$ m s $^{-1} \approx 4v_e$. For $v_{\parallel} > 3 \times 10^6$ m s $^{-1}$, $\eta_K(v_{\parallel})$ decreases again. We can determine the limit as $\eta_K(v_{\parallel} \rightarrow \infty) = (B_2/(B_2 - B_1))^{-\kappa}$, which is about 0.177 for our choice of parameters. This shows that in the theory with kappa functions the reflection of electrons becomes effective for v_{\parallel} on the order of two or three times the local electron thermal speed and larger. The difference between the results for Maxwellian and kappa distribution is due to the relative lack of electrons with large v_{\parallel} for the Maxwellian distribution.

[26] It is not a contradiction that the areas below the curves of $\eta_M(v_{\parallel})$ and $\eta_K(v_{\parallel})$ do not have a unit value, since reflection efficiencies are not to be confused with distribution functions. Reflection efficiencies denote the probability of a reflection of an electron for each value of v_{\parallel} individually, assuming that electrons with this v_{\parallel} exist in the distribution.

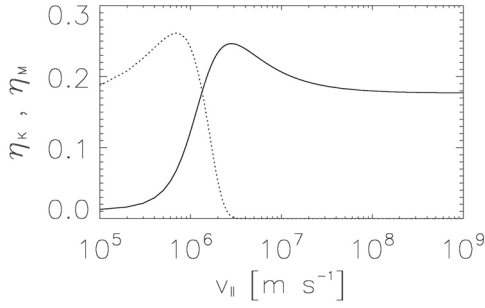


Figure 3. Reflection efficiencies η_M (dotted line) for Maxwellian distributions and η_K (solid line) for kappa distribution functions. While η_M is centered around the thermal electron speed, η_K is largest for large $v_{||}$. Parameters used are $\kappa = 2.5$, $T_e = 3 \times 10^4$ K, $B_1 = 4$ nT, $B_2 = 8$ nT, $v_d = 700$ km s $^{-1}$, and $\theta_{bn} = 45^\circ$, resulting in $v_e = 674$ km s $^{-1}$, and $v_c = 700$ km s $^{-1}$.

[27] Figure 4 shows the reflected reduced electron distribution $F_{rK}(v_{||})$ (solid line), predicted by (17) for an upstream kappa electron velocity distribution, and $F_{rM}(v_{||})$ (dotted line), predicted by (1), (5) and an upstream Maxwellian electron velocity distribution. Both distributions are in the de Hoffman-Teller rest frame of the shock. We see that $F_{rK}(v_{||})$ peaks near a value $\sim 1.2 \times 10^{-8}$ s m $^{-1}$ at the cutoff speed v_c . Then, $F_{rK}(v_{||})$ decreases continuously and approaches the $v_{||}$ axis very slowly for large $v_{||}$.

[28] In comparison, $F_{rM}(v_{||})$ has a local maximum of about 2.16×10^{-7} s m $^{-1}$ at $v_{||} \approx 9 \times 10^5$ m s $^{-1} \approx 1.5v_e$, well above $F_{rK}(v_{||})$. For larger values of $v_{||}$, $F_{rM}(v_{||})$ decreases faster than $F_{rK}(v_{||})$, being practically zero for $v_{||} > 2.4 \times 10^6$ m s $^{-1}$. In contrast, for $v_{||} > 2.4 \times 10^6$ m s $^{-1}$, $F_{rK}(v_{||})$ has still significant values and extends in a very elongated high $v_{||}$ tail.

[29] This shows that in the case of a Maxwellian distribution significant numbers of beam electrons have parallel speeds up to a few times the cutoff speed, where the average speed of the beam electrons is slightly above the cutoff speed for these parameters. For a kappa distribution there are fewer beam electrons with speeds near a few times v_c , but

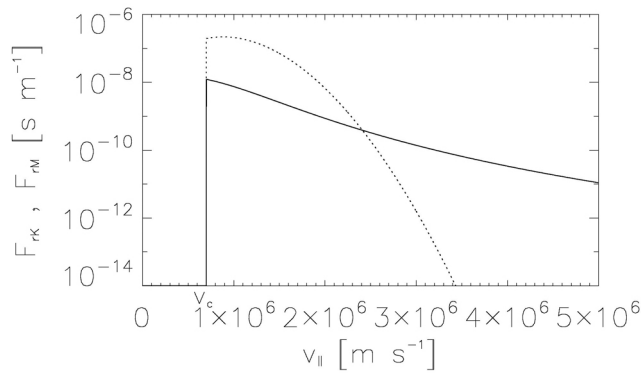


Figure 4. Beam distributions $F_{rM}(v_{||})$ (dotted line) and $F_{rK}(v_{||})$ (solid line) for incident Maxwellian and kappa distributions, respectively. While $F_{rM}(v_{||})$ is practically zero above a few v_c , $F_{rK}(v_{||})$ exhibits a very elongated high velocity tail.

significant numbers of beam electrons with much higher $v_{||}$. Thus, incident kappa electron distributions are more effective in producing higher energy electrons, even though the relative energy gain is unchanged for a given $v_{||}$, since the kappa distribution has more high $v_{||}$ particles than the Maxwellian [e.g., *Knock et al.*, 2003a].

3. Plateauing Results

[30] The reflected electron beam distribution constitutes a “bump” on the tail of the background electron distribution that can drive Langmuir waves via the conventional beam or “bump-on-tail” instability [see, e.g., *Filbert and Kellogg*, 1979; *Cairns*, 1987b]. The instability is driven by a positive gradient $\partial F_r(v_{||})/\partial v_{||}$ of the reduced electron distribution function $F_r(v_{||})$, and the growth rate is proportional to the value of $\partial F_r(v_{||})/\partial v_{||}$ at the wave phase speed. The energy for the Langmuir waves to grow comes from the electron beam. This energy extraction causes beam electrons to move toward lower kinetic energy and $v_{||}$. Quasilinear theory treats the relaxation of the electron distribution function and the growth of the waves quantitatively (see, e.g., the review of *Melrose* [1985]). Assuming spatial homogeneity and a delta function beam, quasilinear theory predicts that the system evolves to a state in which 2/3 of the initial beam kinetic energy $\frac{1}{2}m_e n_b v_b^2$ goes to the waves and 1/3 is retained by the electrons, whose distribution function is flattened into a plateau in $v_{||}$ space [*Melrose*, 1985]. This plateau has $\partial F_r(v_{||})/\partial v_{||} = 0$, and thus the growth rate for Langmuir waves vanishes. Warm beams have less energy available for wave growth, now with the estimate $\approx \frac{1}{2}m_e n_b v_b \Delta v_b$ [*Melrose*, 1985; *Robinson et al.*, 1994; *Robinson and Cairns*, 1995].

[31] Figure 5 shows the configuration in velocity space of the quasilinear plateauing effect. The reflected electron beam distribution $F_r(v_{||})$ given by (16), starts from the cutoff speed v_c and is superposed on the reduced distribution $F_i(v_{||})$ of the background electrons given by (14). The total electron distribution $F_T(v_{||}) = F_r(v_{||}) + F_i(v_{||})$ has $\partial F_T(v_{||})/\partial v_{||}|_{v_{||}=v_c} > 0$ for the steep rise starting at v_c and is unstable to the growth of Langmuir waves with phase speed v_ϕ . Such electrons lose energy, moving to lower $v_{||}$ and reducing the

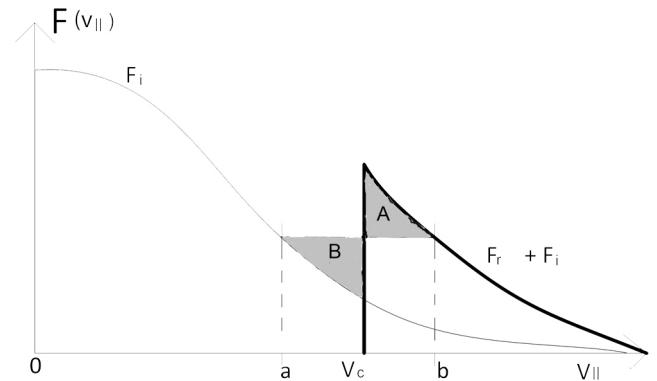


Figure 5. Configuration of electron distributions and the plateauing effect. The generation of Langmuir waves erodes the peak of the total distribution $F_r(v_{||}) + F_i(v_{||})$ and leads to a flat plateau between parallel speeds a and b for which the areas $A = B$ due to particle number conservation.

slope $\partial F_T(v_{\parallel})/\partial v_{\parallel}|_{v_c}$ and so the Langmuir growth rate. This conversion process comes to an end when the peak of $F_T(v_{\parallel})$ is eroded completely, leading to a plateau with $\partial F_T(v_{\parallel})/\partial v_{\parallel} = 0$ in the regime to the left of and adjacent to the eroding peak. The energy for the excited Langmuir waves is taken from the electrons with $\partial F_T(v_{\parallel})/\partial v_{\parallel} > 0$ in the beam velocity distribution.

[32] The corresponding plateau is indicated in Figure 5 as the horizontal line between the values a and b on the v_{\parallel} axis. As the waves grow, electrons with v_{\parallel} such that $\partial F_T(v_{\parallel})/\partial v_{\parallel} > 0$ lose energy and move into the plateau for which $a \leq v_{\parallel} \leq v_c$, $\partial F_T(v_{\parallel})/\partial v_{\parallel} \approx 0$, and the growth rate is close to zero. The total number of the electrons is conserved in this process. Then the plateau has the property that the area A for $v_{\parallel} > v_c$ is equal to the area B for $v_{\parallel} < v_c$. This property can be used to calculate the edges a and b of the plateau explicitly, as outlined in Appendix B. The analytic formulae for a and b depend on the shock parameters and the background electron distribution. Once a and b are known, we obtain the beam density, beam velocity and beam width [Knock et al., 2001, 2003a, 2003b; Knock and Cairns, 2005; Schmidt and Gopalswamy, 2008] as

$$n_b = F_i(a)(b - a), \quad v_b = \frac{1}{2}(a + b), \quad \Delta v_b = b - a. \quad (18)$$

These beam parameters enter the analytic theory of Robinson and Cairns [1998a, 1998b] for the calculation of the radio emissivities and flux, which we summarize in the next section.

[33] Mapping of the calculated beam, Langmuir, and radio wave properties in the foreshock proceeds as follows. At each point outside the shock front, starting just upstream of the shock, we determine the path of the electron beam in the solar frame using

$$\mathbf{v}_{path} = v_b \mathbf{b} + \mathbf{v}_d, \quad (19)$$

where $\mathbf{b} = \mathbf{B}/|\mathbf{B}|$ is the unit vector of the magnetic field, and \mathbf{v}_d is the local $\mathbf{E} \times \mathbf{B}$ drift velocity. Reconstructing the paths of the electron beams yields a mesh of lines covering the upstream region of the shock, on each of which we compute the radiation excited. Dynamic spectra are then constructed by taking the volume emissivity of each cell in the radiation field times the volume of that cell and summing over all cells, taking into account travel to the observer, as described in Section 4.

4. Growth of Langmuir and Radio Waves

[34] As summarized in Section 3 and elsewhere, electrons can be energized by shock wave acceleration in a highly structured and temporally evolving plasma. When the beam speed v_b of the accelerated electrons exceeds about two times the thermal speed of the electrons, Langmuir plasma waves L can be excited efficiently via the beam plasma instability [e.g., Melrose, 1985].

[35] There are three nonlinear processes considered to produce radio emission at f_p and $2f_p$ [e.g., Cairns and Melrose, 1985; Nelson and Melrose, 1985; Cairns, 1987b; Robinson and Cairns, 1998a; Knock et al., 2001; Cairns, 2011]. (1) The beam-driven Langmuir waves L produce backscattered Langmuir waves L' and ion acoustic waves S

via electrostatic (ES) decay: $L \rightarrow L' + S$. (2) Stimulated by the ES decay products S , L waves decay into radio waves T just above f_p and ion acoustic waves S' via electromagnetic (EM) decay: $L \rightarrow T(f_p) + S'$. (3) The coalescence of beam-driven L and backscattered L' Langmuir waves produce radio waves just above $2f_p$: $L + L' \rightarrow T(2f_p)$. Decay processes are thought to be more likely than coalescence processes, since decay processes require only a single population of nonthermal waves to produce nonthermal product waves, whereas coalescence processes require both participating populations to be nonthermal [e.g., Cairns and Melrose, 1985, and references therein].

[36] Stochastic growth theory (SGT) takes the ideas of inhomogeneities and incomplete quasilinear relaxation several steps further [e.g., Robinson, 1992; Robinson et al., 1993b; Cairns and Robinson, 1997, 1999; Robinson et al., 2004, 2006]. It assumes that a wave-particle system is very close to a state of marginal stability when averaged over time and volume. Further, the wave gain $G(t) = \ln(E(t)/E_0) = \int_{-\infty}^t \gamma(t) dt$ is assumed to be a stochastic variable. Here $E(t)$ is the wave electric field at time t , E_0 is a reference field, and $\gamma(t)$ is the Langmuir growth rate. This leads to the waves being intrinsically bursty. Also, the logarithmic dependence of G on the wavefield enables a qualitative explanation of the production of waves with a wide range of wavefields, from quasithermal to those approaching or exceeding the thresholds for nonlinear processes. Presupposing that many fluctuations in γ and G occur during some characteristic time for the waves, then the Central Limit Theorem predicts that the probability distribution G (and so $\log E$) will be a Gaussian [e.g., Robinson, 1992]. This feature has been validated in a large number of applications [e.g., Cairns and Robinson, 1997, 1999; Robinson et al., 2004, 2006].

[37] In one model for achieving an SGT state for electron beam-driven Langmuir waves the beam moves through an inhomogeneous plasma which has multiple evolving sites where wave growth is favored. This leads to enhanced localized growth and modification of the particle distributions inside the sites, while the beam rebuilds between growth sites due to faster electrons outrunning slow ones and increasing $\partial F_T(v_{\parallel})/\partial v_{\parallel}$ [e.g., Robinson, 1992; Robinson et al., 1993b; Cairns and Robinson, 1997].

[38] In addition, SGT provides a quantitative prediction for the amount of energy entering the Langmuir waves irrespective of the details of the wave growth and saturation. In detail, the total time derivative of the free energy available from quasilinear relaxation of the electron beam equals the power flux entering the Langmuir waves, yielding in steady state [e.g., Robinson et al., 1994; Knock et al., 2001]

$$\frac{d}{dt} W_L = \mathbf{v} \cdot \frac{\partial}{\partial \mathbf{r}} \left(\frac{n_b v_b \Delta v_b}{3} \right) \approx \frac{n_b v_b^2 \Delta v_b}{3l}. \quad (20)$$

[39] In (20) $W_L = \epsilon_0 E_L^2/2$ is the electric energy in the Langmuir waves with the permittivity of free space ϵ_0 , and the factor 3 comes from multiplying the quasilinear prediction that 2/3 of the initial available kinetic energy reaches the waves with the 1/2 for the definition of kinetic energy. The approximation in (20) includes replacing the derivative with

v_b/l , where l is the distance from the shock to the observer location along the trajectory for $v_{\parallel} = v_b$ [Knock *et al.*, 2001].

[40] Using SGT, Robinson and Cairns [1998a, 1998b] derived volume emissivities j_M for the fundamental ($M = F$) and second harmonic ($M = H$) plasma radiation produced by the above nonlinear processes from Langmuir waves excited by an electron beam. In particular, they found

$$j_M(\mathbf{r}) \approx \frac{\Phi_M}{\Delta\Omega_M} \frac{n_b m_e v_b^3}{3l(r)} \frac{\Delta v_b}{v_b}, \quad (21)$$

where $\Delta\Omega_M$ is the solid angle over which the emission is spread, i.e., $\Delta\Omega_F = \pi/4$ and $\Delta\Omega_H = 2\pi$ [see, e.g., Knock *et al.*, 2001], n_b is the beam number density, v_b is the beam speed, $l(r)$ is the distance along the beam path from the shock to the location \mathbf{r} at heliocentric distance r , and Δv_b is the width of the beam distribution in velocity phase space. The conversion efficiencies for fundamental and harmonic radiation via the foregoing nonlinear Langmuir processes are [Robinson *et al.*, 1994; Robinson and Cairns, 1998b; Dulk *et al.*, 1998; Knock *et al.*, 2001; Mitchell *et al.*, 2004]

$$\Phi_F \approx 72\sqrt{3} \frac{\gamma_L}{\gamma_S} \frac{v_e^3}{c^3} \frac{v_b}{\Delta v_b} \frac{e^{-u_e^2}}{u_c \sqrt{\pi}} \zeta_F, \quad (22)$$

$$\Phi_H \approx \frac{18\sqrt{3}}{5\gamma_t} \sqrt{\frac{m_i}{\gamma_i m_e}} \frac{v_b^2 v_e^3}{c^5} \frac{v_b}{\Delta v_b} \zeta_H, \quad (23)$$

respectively. The expressions involving u_c in (22) are the escape factor for fundamental radiation subject to scattering by density irregularities and absorption by linear mode conversion, where $u_c = 2.1$ is a typical value [e.g., Robinson and Cairns, 1998a]. Also, γ_L/γ_S is the ratio of the damping rates of the product waves in the electrostatic Langmuir wave decay process, $\gamma_t = 1 + 3T_i/T_e$, where T_i is the ion (proton) temperature, m_i is the mass of the ions, and the ζ_M factors are the respective fractions of Langmuir waves that are kinematically able to contribute to the fundamental ($M = F$) and harmonic emission ($M = H$). In more detail,

$$\zeta_F \approx \exp \left[-\frac{4\gamma_t m_e}{45m_i} \left(\frac{v_b}{\beta \Delta v_b} \right)^2 \left(\frac{3}{2} \sqrt{\frac{m_i}{\gamma_i m_e}} - \frac{v_b}{v_e} \right)^2 \right], \quad (24)$$

$$\zeta_H \approx \frac{c}{2v_b} \sqrt{\frac{\pi \beta \Delta v_b}{6}} \frac{1}{v_b} \cdot \left[\operatorname{erf} \left(\frac{v_e \sqrt{3}}{c} + \frac{2}{3} \sqrt{\frac{\gamma_i m_e}{m_i}} \right) + \operatorname{erf} \left(\frac{v_e \sqrt{3}}{c} - \frac{2}{3} \sqrt{\frac{\gamma_i m_e}{m_i}} \right) \right], \quad (25)$$

where $\beta \approx 1/3$ is the width of the model beam-driven Langmuir spectrum, which ensures that this spectrum is negligible outside the range of beam-driven wave vectors [e.g., Knock *et al.*, 2001]. In the case $3 \leq T_e/T_i \leq 5$, $\gamma_L/\gamma_S \approx (80/7)(v_e/v_b)^2 \sqrt{(m_i/7m_e)}$ [e.g., Knock *et al.*, 2001]. For the coronal plasma $T_e/T_i = 3$ is assumed in this paper.

[41] Using the volume emissivities j_M , the flux density of radiation into mode M is given by integrating over the source

and accounting for propagation of the radiation from the source to the observer at \mathbf{r}_0 [e.g., Cairns, 2011]:

$$F_M(f, t, \mathbf{r}_0) = \sum_{t'} \frac{\Delta\Omega_M}{\Delta f_M} \int d^3r \frac{j_M(f, \mathbf{r}, t')}{|\mathbf{r} - \mathbf{r}_0|^2}, \quad (26)$$

where

$$t = t' + \int \frac{d\tau}{v_g(\mathbf{r})} \approx t' + |\mathbf{r} - \mathbf{r}_0|/c \quad (27)$$

is the time at the observer, which is the sum of the emission time t' and the time $\int d\tau/v_g(\mathbf{r})$ a radio wave with group velocity $v_g(\mathbf{r})$ needs to reach an observer along a trajectory with line elements $d\tau$. Quantities $\Delta f_F = 3(v_e/v_b)^2(\Delta v_b/v_b)$ and $\Delta f_H = 12(v_e/v_b)^2(\Delta v_b/v_b)$ are the corresponding intrinsic bandwidths of radiation. In the case that the radiation source is localized and the distance between the source region and the observer is large; e.g., a satellite at Earth's orbit observes a radio source in the corona of the Sun, $|\mathbf{r} - \mathbf{r}_0|$ can be treated as a constant. In the example below $|\mathbf{r} - \mathbf{r}_0| \approx 1$ AU. The summation procedure includes an inverse square dependence on the distance to the observer for each cell and a bandwidth factor arising from the conversion from energy to flux. The procedure does not include possible refraction and intrinsic angular and spatial diffusion effects for the radiation propagating in the interplanetary medium, as discussed by Cairns [2011]. Instead there is only straight line propagation to the observer of emission that escapes without further absorption once outside the source. Importantly, though, the theory of Robinson and Cairns [1998a, 1998b] for fundamental emission includes losses due to scattering and absorption in the near vicinity of the source. In order to obtain time-dependent dynamical spectra, the summation is repeated for each time step in the simulation.

5. MHD Model

[42] The MHD code used is based on the algorithms described by Zalesak [1979] and DeVore [1991] for a flux-corrected transport (FCT) scheme for solving the MHD equations, meaning that the MHD equations are solved in conservative form as first order partial differential equations for the fluxes, which are functions of the physical variables density ρ , velocity \mathbf{v} , magnetic field \mathbf{B} , and pressure p . The accuracy reached in this code is fourth order accuracy in space and second order accuracy in time. The code thus conserves $\nabla \cdot \mathbf{B} = 0$ to machine accuracy. Successful applications include the works by Cargill *et al.* [2000], Schmidt and Cargill [2001, 2003, 2004], and Schmidt and Gopalswamy [2008]. The sharpness of shocks is well preserved in such schemes; see for instance Cargill *et al.* [2000, Figure 5], with a shock followed up to 5.6 AU. In the version of the code used here, the MHD equations are solved in spherical coordinates r and θ , where a rotational symmetry around the rotation axis z of the Sun is assumed; i.e., all fields are considered to be independent of the azimuthal coordinate ϕ . Yet, since all vector fields still have three components, the code is $2\frac{1}{2}$ dimensional.

[43] The computational grid consists of 300×100 points in the $r - \theta$ plane, in which the radial extension of the simulation box is from R_{\odot} to $4R_{\odot}$ from the origin at the

Sun's center. In Figure 6, $x = r \sin \theta$ denotes the in-ecliptic coordinate, $z = r \cos \theta$ the spatial coordinate out of the ecliptic plane, and thick dashed lines show the boundaries of the simulation box at $\theta = 9.7^\circ$ and $\theta = 170.2^\circ$. At the sides with meridional angles $\theta = 9.7^\circ$ and $\theta = 170.2^\circ$ and the outer boundary at $4 R_\odot$, the boundary conditions are floating, which means that a disturbance at that boundary can leave the simulation box without being reflected. We specify the density ρ , velocity \mathbf{v} , magnetic field \mathbf{B} and the pressure p of the solar wind throughout the domain above $1 R_\odot$ for the initial state, obtaining the current density \mathbf{j} by using the curl of \mathbf{B} . The values of these quantities are kept constant at the inner boundary at $1 R_\odot$ throughout the simulation. In particular, the initial solar wind is introduced as a radial Parker wind, which reaches a radial speed of about 200 km s^{-1} at $4 R_\odot$ heliocentric distance. The pressure follows an adiabatic law $p = p_0(\rho/\rho_0)^\gamma$, where p_0 and ρ_0 are values at a reference point, and the polytropic index $\gamma = 5/3$. This law assumes a coronal temperature of 1.2 MK at $r = R_\odot$ and a number density $n_0(R_\odot) = 3.3 \times 10^{14} \text{ m}^{-3}$ for a Parker density profile, which are typical values for the solar corona [see, e.g., *Aschwanden*, 2004]. These values correspond to $p \approx 5.5 \times 10^{-3} \text{ Pa}$ and $2f_p \approx 326 \text{ MHz}$ at $r = R_\odot$. The polytropic index γ switches from $5/3$ to 1 if the pressure is close to zero or the location is within a rarefaction region like the CME [see, e.g., *Cargill et al.*, 2000]. This procedure exploits the finding that the very thin coronal plasma should behave nearly isothermally (if heating sources are ignored), which inhibits pressure fluctuations that would lead to negative pressure values for a calculation on a truncated grid.

[44] A CME is introduced as a flux rope of cylindrical shape that extends like a torus around the z axis and is embedded in an appropriately distorted radial solar magnetic field. This initial state is not modeled by superposing the flux rope and a pure radial magnetic field, which would be a configuration with jumps containing unphysical magnetic monopoles. Rather, a smooth exact solution of the magnetostatic Maxwell equations is used for this configuration [*Schmidt*, 2000]. CMEs with a flux rope geometry are a subclass of observed CMEs [see, e.g., *Cremades and Bothmer*, 2004; *Forbes et al.*, 2006]. Initially, the center of the flux rope is at $r = 1.38 R_\odot$ in the ecliptic plane, and its initial radial speed and diameter are 100 km s^{-1} and $0.61 R_\odot$. The magnetic field strength varies strongly with position along the inner boundary of the simulation box at $r = R_\odot$. At $\theta = 9.7^\circ$ and $\theta = 170.2^\circ$ $B = 2 \text{ G}$ (0.2 mT) on this boundary but increases toward $\theta = 90^\circ$, reaching a peak value of 400 G (40 mT) at $\theta = 90^\circ$ and $r = R_\odot$. This peak value is typical for foot point magnetic fields in active regions [see, e.g., *Aschwanden et al.*, 1999]. Within the simulation box, the magnetic field strength is about 4 G (0.4 mT) around the body of the CME, and is 16 G (1.6 mT) along the symmetry axis in the middle of the flux rope. The initial internal pressure of the CME is increased by a factor of three with respect to the external solar wind pressure, according to measurements of overexpanding CMEs [e.g., *Gosling et al.*, 1998].

[45] Figure 6a shows the magnetic field line configuration of the erupting flux rope 20 min after launch, using a contour plot of the quantity $A_\phi r \sin \theta$ where A_ϕ is the ϕ -component of the vector potential. This figure displays a projection of the

flux rope's twisted magnetic field lines onto a cross section of the x - z plane (see Appendix C for a derivation showing that the lines shown, which satisfy $A_\phi r \sin \theta = \text{constant}$, are magnetic field lines within the x - z plane provided that \mathbf{B} has no ϕ -dependence). These projections are nearly circular and have an anti-clockwise sense of rotation. This flux rope is embedded in a radial magnetic field, originating from the solar surface and directed away from the Sun. Here, full lines correspond to positive values of the vector potential and dashed lines to negative values. Since the outer magnetic field has an opposite sense to the rope's magnetic field in the northern hemisphere, we find a point with two exactly anti-parallel and reconnecting magnetic field lines at the northern edge of the flux rope. The characteristic "necking" shape of magnetic field lines at a x -point reconnection region is clearly visible. This configuration with an external radial unipolar field corresponds to a coronal hole type of CME configuration. A possible alternative magnetic field configuration is a streamer-type CME configuration, which has a field configuration that is opposite on opposite sides of the rope, thus having no flank reconnection. In the latter case the magnetic field configuration in the northern half of the simulation box would be a mirror image of the magnetic field configuration of the southern half of the simulation box with reversed direction of the magnetic field.

[46] Due to the outward motion and expansion of the CME, the radial magnetic field of the Sun is distorted around the body of the CME. We see an increase of the number density of the field lines in a roughly ellipsoidal area enshrouding the body of the CME, corresponding to an increase in B and to magnetic draping. The fringe of this ellipsoidal area of increased number density of field lines, where there is a substantial rotation of \mathbf{B} , is the front of the shock driven by the CME. We detect that the magnetic field lines intersect the shock front at angles close to 90° with respect to the shock normal \mathbf{n} on the northern (upper) and southern (lower) flanks of the shock. In contrast, near the nose of the shock, where $x \approx 2.5 R_\odot$, the angle θ_{bn} between \mathbf{B} and the local \mathbf{n} is small. Thus, we expect the electron acceleration to be most effective at the northern and southern flanks of the shock. Yet there is still acceleration of electrons in the nose region of the shock. These properties should lead to more intense radio signals at the northern and southern flanks of the shock and a smaller radio signal at the nose of the shock [e.g., *Knock et al.*, 2001, 2003a, 2003b; *Cairns et al.*, 2000; *Cairns*, 2011]. We discuss the radiation arising at the more complicated situation of radiation arising at the northern and southern flanks to a companion paper.

[47] Figure 6b shows the entropy gradient $|\nabla(p/\rho^\gamma)|$ in the simulation box, where p and ρ are the pressure and density calculated by the MHD code. The entropy jumps at the edge of the ellipsoidal area. This edge was already identified as the shock front in its nose region in Figure 6a. The entropy jump provides a sharper definition of the location of the shock front than the contour plot; even so, higher resolution studies of the shock front are necessary in the companion paper. In the middle of the ellipsoidal area, within the body of the CME and the surrounding downstream "sheath" region, the entropy fluctuates, indicating energy flows triggered with the varying fields in the eruption.

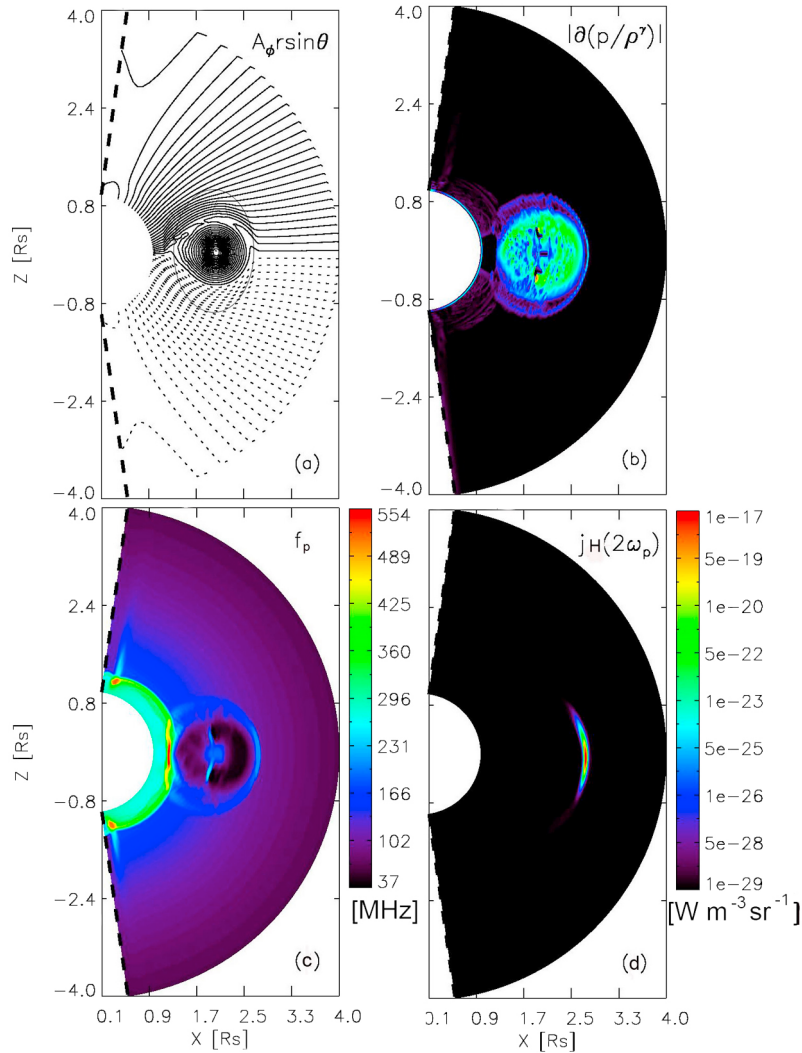


Figure 6. MHD and radiation simulation results 20 min after the launch of the CME. (a) Field line pattern in and around the CME in the x - z plane that has a reconnection site at the northern edge of the CME. The front part of the ellipse roughly denotes the location of the shock. (b) The gradient of the entropy. (c) The plasma frequency f_p is increased within a ring that follows the ellipsoidal curve of the shock. (d) Map of the harmonic plasma emissivity j_H .

[48] Figure 6c shows the spatial variations of f_p in the simulation box, which is proportional to the square root of the density. We find a ring of increased f_p roughly along the ellipsoidal line already identified as a marker of the shock front in Figures 6a and 6b. This ring shows the increase in density expected downstream of the shock. The maximum change in density is expected at the shock ramp, although spreading of the ramp over several MHD grid cells is expected due to imprecisions of the calculation on a truncated grid. We find that the position of the entropy jump is roughly in the middle of that ramp.

6. Shock Identification

[49] In this paper we use the entropy jump to determine the location of the shock near the nose (most distant) region of the CME. In the companion paper a more general technique

is described for determining the shock position precisely, which also works for uneven and rippled shock surfaces. Here we fit an ellipsoidal curve

$$\left(\frac{x-x_0}{A}\right)^2 + \left(\frac{z-z_0}{B}\right)^2 = 1 \quad (28)$$

to the ellipsoidal area identified in Figure 6b, where A and B are the minor and major axis of the ellipse. The focus (x_0, z_0) of the ellipse is determined as the midpoint of the rarefaction region due to overexpansion of the CME, which can be seen in Figure 6c. The ellipse parameters were then determined by hand from analogs of Figure 6b for each MHD timestep. For the specific case in Figure 6b at $t = 20$ minutes after the launch of the CME, the parameters are $x_0 = 1.91 R_\odot$, $z_0 = 0.00 R_\odot$, $A = 0.74 R_\odot$ and $B = 1.05 R_\odot$. This ellipse is taken to be the shock front, and we use the normal to the

ellipse as the shock normal, which is directed almost radially near the nose. If

$$\left(\frac{x-x_0}{A}\right)^2 + \left(\frac{z-z_0}{B}\right)^2 > 1, \quad (29)$$

for a point (x, z) taken in the simulation box, then that point is outside the ellipse and therefore upstream of the shock. We take the upstream plasma parameters from several grid cells upstream of the shock in order to avoid possible irregularities associated with the shock transition itself. The paths of the electron beams are approximately given by the normal direction in this case since \mathbf{B} is almost radial. Occasionally the ellipse is not a good fit and the ellipse lies in the downstream region. Since downstream cells should not produce radio emission [Cairns, 2011], cells that are in front of the ellipse but are within or downstream of the actual shock ramp (according to the density values) are left out of the calculation of the radio emissivities.

[50] This suppression of downstream radiation is required for experimental reasons as follows. Cairns [1986b] first claimed the existence of fundamental upstream f_p radiation and showed definitively that the harmonic $2f_p$ signals are transverse electro-magnetic radiation generated in the foreshock in the free-space modes, using (1) the simultaneous observation of harmonic radiation from regions with different densities present simultaneously in the foreshock, (2) the persistence of the signals into the undisturbed solar wind and other regions of the foreshock, (3) the inability of electrostatic modes to propagate significant distances, and (4) the free-space mode being the only essentially undamped mode significantly above f_p in a stable plasma like the solar wind. Burgess *et al.* [1987] showed definitively that f_p radiation is also produced in Earth's foreshock, using the same arguments as (1)–(4) above but for f_p radiation. Another argument for the radiation source being the (3-D) foreshock is based on “direction finding”. Early workers [Hoang *et al.*, 1981; Cairns, 1986b] used a single spacecraft to establish consistency with the foreshock, while Reiner *et al.* [1997] used direction-finding with two spacecraft to triangulate the radio source and found it to be in the foreshock. A final argument for $2f_p$ radiation being generated in the foreshock comes from the observed spatial variations in intensity. Specifically, Lacombe *et al.* [1988] and Kasaba *et al.* [2000] found that the $2f_p$ radiation has its largest fields relatively close to the upstream boundary of the foreshock, in approximate coincidence with the largest fields of Langmuir waves, and not in the solar wind or the deep foreshock. This is expected if the radio source lies in the foreshock and is associated with the Langmuir waves or their driving electron beams.

[51] A theoretical argument against emission from downstream of a single shock is the lack of suitable electron beams to generate strongly nonthermal Langmuir waves and radio emission. For the ideal shocks considered here, with no magnetic overshoot, there is no magnetic mirror for downstream electrons going upstream, and so the only downstream electron beams are associated with the cross-shock potential reflecting downstream electrons or pulling upstream electrons downstream. Such beams have kinetic energies less than or equal the cross-shock potential, which is of order several times the upstream electron thermal energy [Kuncic *et al.*,

2002]. The downstream electrons are hotter than the upstream electrons, so that these relatively slow beams have speeds less than several electron thermal speeds and so should be ineffective in driving Langmuir waves. Consistent with this, only quasithermal types of Langmuir waves are found within the ramps and downstream regions of shocks [Onsager *et al.*, 1989].

7. Dynamic Spectrum Results

[52] Figure 6d shows the mapped source region for harmonic radiation emitted in front of the nose of the CME shock, using the volume emissivity j_H predicted using the new analytical model in sections 3–6. The radiation field has a crescent or sickle-like shape in front of the shock front, which is slightly more extended to the north than to the south. The maximum volume emissivity of radiation is about $10^{-17} \text{ W m}^{-3} \text{ sr}^{-1}$ near the nose of the shock, with a maximum slightly above the ecliptic plane, and a decrease of the radiation emissivity toward the northern and southern edges of the sickle-shaped radiation field, and with increasing radial distance from the shock.

[53] The small asymmetry between the northern and southern hemisphere in Figure 6d is caused primarily by the asymmetry in the magnetic field line pattern, which has a reconnection site at the northern edge of the CME. This asymmetry leads to slightly larger intersection angles of the magnetic field lines with the shock normals in the northern hemisphere than in the southern hemisphere near the nose. This should cause variations in the reflected electron beam parameters and radiation as discussed further below.

[54] Figure 7 shows the flux density given by (26) as a function of frequency and time derived from analogs of Figure 6d for both fundamental and harmonic emission. For the thickness of the source in the y direction we assume one grid cell, which is $10^{-2} R_\odot$. Data are taken from the complete simulation run that spans a time up to 50 min after the launch of the CME. Figure 7 shows a sharp lower (higher) frequency band that drifts to lower frequency with increasing time for fundamental (harmonic) radiation in the range $\approx 50 - 80 \text{ MHz}$ ($\approx 80 - 150 \text{ MHz}$). The fundamental and harmonic flux densities are around $2 \times 10^{-18} \text{ W m}^{-2} \text{ Hz}^{-1}$ and $10^{-20} \text{ W m}^{-2} \text{ Hz}^{-1}$, respectively, with $10^{-22} \text{ W m}^{-2} \text{ Hz}^{-1}$ equaling one solar flux unit (sfu). Typical values of observed flux densities are $F = 10^{-18} \text{ W m}^{-2} \text{ Hz}^{-1}$ at $f_p \sim 80 \text{ MHz}$ [e.g., Holman and Pesses, 1983]. The observed flux densities discussed by Lobzin *et al.* [2008] for type II radio bursts are also comparable to our simulated flux densities. Further, the type II event observed by Bale *et al.* [1999] and simulated by Cairns and Knock [2006] has maximum flux densities $F_F \sim 10^{-18} \text{ W m}^{-2} \text{ Hz}^{-1}$ and $F_H \sim 10^{-20} \text{ W m}^{-2} \text{ Hz}^{-1}$ at frequencies from $\sim 10^5 \text{ Hz}$ to $\sim 10^6 \text{ Hz}$. Thus, our simulated emissions have fluxes that are broadly consistent with the observations.

[55] In Figure 7 we can also see the fundamental and harmonic bands fading out and then reappearing, with the gap being between times 21 and 24 min. Figure 8a, taken from Schmidt and Gopalswamy [2008], shows that the acceleration $a(t)$ of the center of the CME (taken as a ballistic object) decreases during that period. The shock travels ahead of the CME and is not subject to the forces that retard the CME. Hence, in the rest frame of the shock the CME has

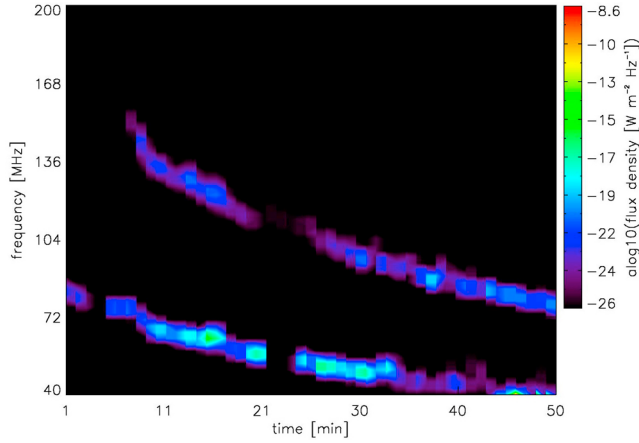


Figure 7. Dynamic spectrum predicted at Earth using (26) from upstream of the shock near the nose of the CME. Maximum flux densities along the bands are $\sim 2 \times 10^{-18} \text{ W m}^{-2} \text{ Hz}^{-1}$.

a diminishing speed as long as the acceleration on the CME is negative. It is this diminished speed of the plasma at the rear of the shock that is correlated next to a weakening of the shock near the nose and thus to the fading of the radio signal.

[56] In Figure 8b we display the ratio of the number densities n_2/n_1 as a function of time after the launch of the CME, where n_2 is taken from the downstream region and n_1 from the upstream region adjacent to the shock in the nose region with $\alpha = 90^\circ$. As explained with Figure 9, α is an azimuthal angular coordinate, measured clockwise from the positive rotation axis z of the Sun, that defines the rotation angle of a pointer centered on the CME's midpoint (x_0, z_0) with length $\sim 0.8R_\odot$ which scans the nose region of the CME-driven shock from north to south. Thus, $45^\circ \leq \alpha \leq 90^\circ$ and $90^\circ \leq \alpha \leq 135^\circ$ correspond to the shock front in the northern and southern hemispheres, respectively (see also Figure 9). The ratio n_2/n_1 is a measurement of the strength of the shock, being closely related to the magnetic jump B_2/B_1 , and has a theoretical maximum value of four for an ideal shock. Hence, if n_2/n_1 and B_2/B_1 are less than four then the shock is not strong, and the shock is weaker the smaller n_2/n_1 and B_2/B_1 become. The shock disappears when $n_2/n_1 = 1$. A weaker shock has a smaller ability to accelerate electrons and thus generate Langmuir waves and radio radiation. Thus, periods with decreased n_2/n_1 in Figure 8 should be where we find less intense radio radiation.

[57] Figure 8 reveals that n_2/n_1 starts just below two around the launching time of the CME and increases to the maximum value of four at about $t = 20$ min. This time interval belongs to the phase where the CME has increasing acceleration and the CME-driven shock develops and becomes steeper and steeper. After $t = 20$ min the CME acceleration in the solar wind frame and the CME speed in the shock rest frame decrease, and we see a sharp drop in n_2/n_1 to a value just slightly above one. (Note that the wiggles on the curve of n_2/n_1 are due to numerical errors on a grid with a limited number of grid points in the temporal dimension.) Hence, the suddenly decreased speed of the CME at the rear of the shock front has led to an almost entire disappearance of the shock at this value of α . The ratio n_2/n_1 remains around one up to about $t = 25$ min. After this time

the CME starts being accelerated again, which is due to growing magnetic buoyancy forces on the flux tube of the CME [see *Schmidt and Gopalswamy, 2008*]. We see a steep increase of n_2/n_1 to a value of about three in Figure 8, near where n_2/n_1 stabilizes for the rest of the simulation. Thus, we find the time interval $t = 21 - 24$ min where the emission bands of the dynamical radio spectra fade out (indicated with the dotted vertical lines in Figure 8), to be in the middle of the period when n_2/n_1 drops to one and the shock essentially disappears. This is consistent with the type II radiation theory.

[58] Figure 10 shows the quantities v_e , v_c , v_b , and θ_{bn} , which are important for the excitation of radio emission, near the nose of the shock at $t = 20$ min. In Figure 10a we display v_c (solid line), v_e (dashed line) and v_b (dashed-dotted line) along the shock front as functions of α . We see that for $\alpha \leq 110^\circ$, $v_c \geq 2v_e$ with $v_b \approx v_c$. This enables the growth of Langmuir waves and so radio emission can be expected.

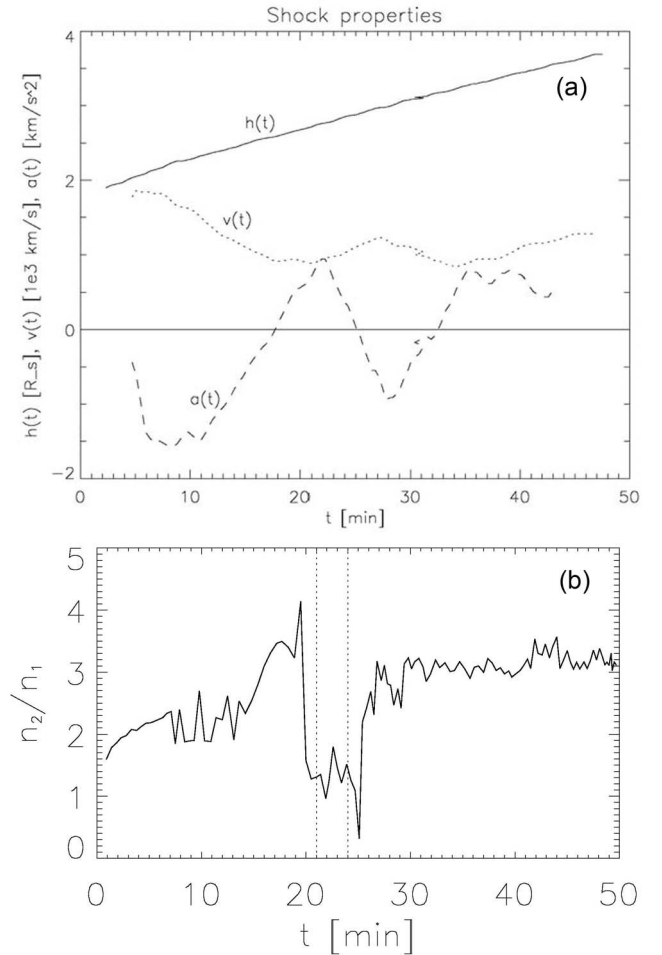


Figure 8. (a) Acceleration $a(t)$, velocity $v(t)$, and height $h(t)$ of the center of the CME taken as a ballistic object [*Schmidt and Gopalswamy, 2008*]. (b) Downstream to upstream ratio n_2/n_1 of number densities at the nose of the shock at $\alpha = 90^\circ$ as a function of time after the launch of the CME. Dotted vertical lines at times 21 and 24 min indicate the period where the emission bands of the dynamic radio spectrum fade away.

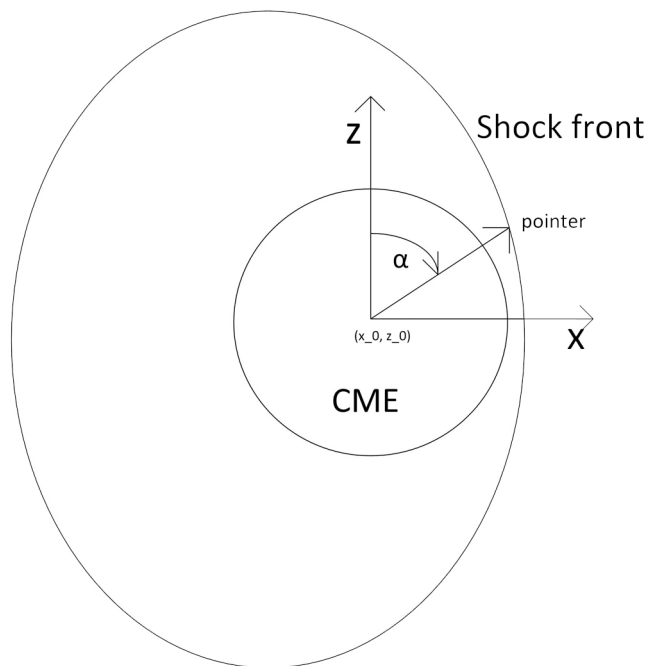


Figure 9. The rotation angle α , measured clockwise from the positive z axis, for a pointer centered on the CME's midpoint (x_0, z_0) that scans points on the CME-driven shock front.

We therefore expect the maximum emission around $\alpha \approx 75^\circ$, where the curves of v_c and v_b peak [cf. *Knock et al., 2003a*].

[59] Figure 11 shows three electron distribution functions at $t = 20$ min for $\alpha = 67^\circ, 79^\circ$, and 91° , predicted in the region upstream of the shock, before quasilinear flattening. The beams are due to reflection by the shock. The $\alpha = 79^\circ$ beam distribution has the largest cutoff speed and a large peak value. Thus, this beam excites the strongest radio emission. The $\alpha = 67^\circ$ distribution has a similar peak height to the $\alpha = 79^\circ$ distribution, yet it has a smaller cutoff speed. This dependence on v_c is why we obtain weaker radio emission

[e.g., *Knock et al., 2003a; Cairns et al., 2003*] as we move in Figure 6d from the $\alpha \approx 75^\circ$ position in the direction of smaller α values. Finally, the $\alpha = 91^\circ$ distribution has a smaller v_c and peak height than the other two beam distributions. This explains why we obtain weaker radio emission if we move from the $\alpha \approx 75^\circ$ position in the direction of larger α values in Figure 6d.

[60] Figure 10b shows θ_{bn} along the shock front as a function of α . In the southern hemisphere $\theta_{bn} \approx 35^\circ$, where $90^\circ \leq \alpha \leq 135^\circ$. If we look at angles α farther to the flanks of the shock than the nose, the electron $\mathbf{E} \times \mathbf{B}$ drift speed v_d decreases, thus leading to decreasing $v_c = v_d \tan \theta_{bn}$ and v_b for $90^\circ \leq \alpha \leq 135^\circ$. On the other hand, $v_e \approx 500 \text{ km s}^{-1}$ is nearly a constant in that α regime. Thus, the strength of the radio source slowly decreases if we move from $\alpha = 90^\circ$ onward toward $\alpha = 135^\circ$ in Figure 6d, since the requirement $v_c \geq 2v_e$ for Langmuir wave excitation is increasingly violated and v_c decreases [e.g., *Knock et al., 2003a; Cairns et al., 2003*].

[61] For $60^\circ \leq \alpha \leq 90^\circ$, $v_e \approx 700 \text{ km s}^{-1}$ is larger than in the southern hemisphere. Thus, the plasma upstream of the shock front in the northern hemisphere is clearly heated relative to the southern hemisphere. This is not due to the shock but instead due to the reconnection site at the northern edge of the CME, where magnetic field energy is set free due to the reconnection of antiparallel magnetic field lines. Hence the shock is produced well after the heated plasma first left the reconnection site and then moves through the hot plasma. The magnetic annihilation influences the magnetic field direction in the vicinity of the reconnection site, leading to the local minimum $\theta_{bn} \approx 40^\circ$ in the angular direction of the reconnection site $\alpha \approx 65^\circ$. Maximum values of θ_{bn} are near 50° at $\alpha \approx 75^\circ$. Again, this double peak feature of the curve θ_{bn} for $60^\circ \leq \alpha \leq 90^\circ$ translates to an equivalent feature of the curves v_c and v_b in the same α regime in Figure 10. On average, v_c and v_b decrease, if we move from $\alpha \approx 75^\circ$ in the direction of smaller α . This explains why the strength of the radio source decreases, if we look in that direction within this α regime (also compare with *Knock et al. [2003a]* and *Cairns et al. [2003]*).

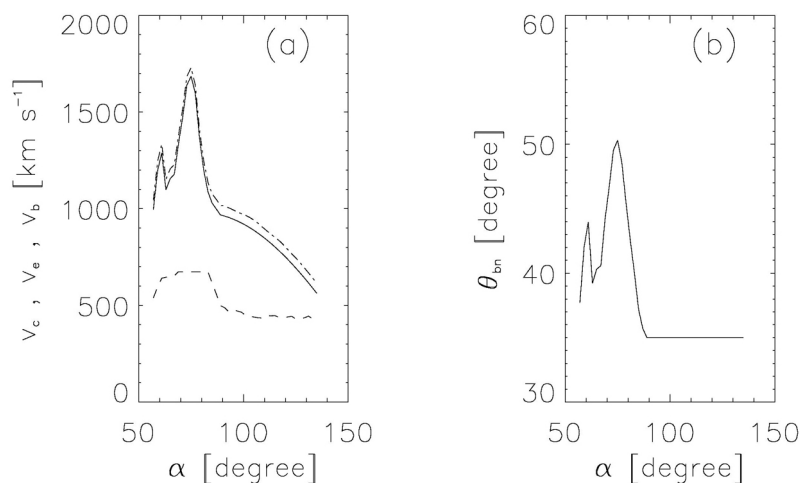


Figure 10. (a) v_c (solid line), v_e (dashed line), and v_b (dashed-dotted line) as functions of α and $t = 20$ min. For $60^\circ \leq \alpha \leq 110^\circ$, $v_c \approx v_b \geq 2v_e$ is well fulfilled, allowing for growth of Langmuir waves and radio excitation. (b) The angle θ_{bn} .

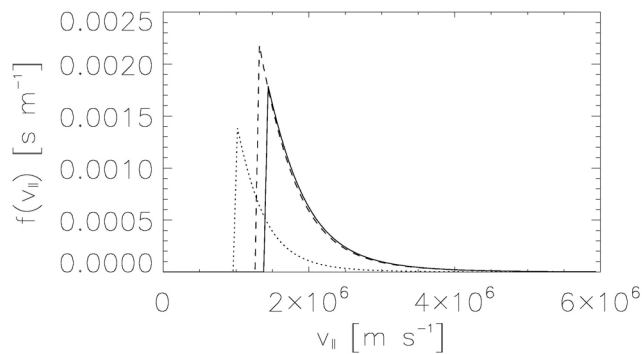


Figure 11. Predicted beam electron velocity distributions (before quasilinear flattening and without the background distribution) at angular positions $\alpha = 67^\circ$ (dashed line), $\alpha = 79^\circ$ (solid line), and $\alpha = 91^\circ$ (dotted line) at $t = 20$ min.

[62] In all, the parameter studies in Figures 10 and 11 let us understand how radio excitation at the nose of the CME-driven shock is possible, and that the radio emission results shown in Figures 6 and 7 are reasonable.

8. Discussion and Conclusions

[63] In this work we revised and extended the work of *Knock et al.* [2001, 2003a, 2003b], *Knock and Cairns* [2005], *Cairns and Knock* [2006], and *Schmidt and Gopalswamy* [2008] related to radio emission excited at CME-driven shocks, extending the foregoing theory with analytic results for the reflection efficiency, intrinsic electron beam distribution functions, and plateaued electron distributions resulting from Langmuir growth for kappa velocity distributions of electrons in the background plasma. Our analytic results yield a kinetic theory for radio emission that can be combined with or bolted onto MHD simulations of CMEs driving shock waves or to other shock simulations (MHD or otherwise) in different coronal or astrophysical systems.

[64] The foregoing calculations correct the work of *Schmidt and Gopalswamy* [2008] to remove downstream emission, extend the emission theory of Knock and collaborators to be fully analytic and to fully include kappa electron distribution functions for the typically nonthermal solar wind electrons, and also show how to better capture the front of the shock in the MHD simulation. In particular, there is no emission arising from the downstream region any longer, which appeared in the previous combined or bolt-on calculations.

[65] The CME and associated radio calculations reported here are only initial work, and are not intended to model particular events or be fully realistic. In particular, plasma temperatures as low as 10^4 K near the nose of the shock are unrealistic for the corona and inner solar wind. We would expect the shock to propagate into a heated coronal and solar wind plasma that has temperatures of order 10^6 K. Higher solar wind temperatures would require higher cutoff speeds at the shock front to produce significant radiation. Other options are to design the CME to be more ballistic with a more elongated ellipsoidal body of the CME in the radial direction rather than a nearly circular body, or to introduce

coronal magnetic field loops or other magnetic structures whose fields are more radial [e.g., *Knock and Cairns*, 2005]. These would make the shock front more quasi-perpendicular and thus increase the cutoff speed and radio emission. Future work will be along these lines.

[66] We also developed a routine to identify the shock location of the CME-driven shock, which detects a sharp jump of the entropy at the shock front in the nose of the shock. The locus of entropy jumps is well approximated with an ellipse that lies in a steep gradient of the density at the shock. With a precise positioning of the shock front, and taking upstream plasma parameters from several grid cells upstream of the ellipse, we are now able to correct the work of *Schmidt and Gopalswamy* [2008] to avoid any unphysical radiation arising from the downstream region. Dynamical spectra now yield sharp drifting bands that are in good qualitative agreement with observations. We can detect occasional fading of the harmonic and fundamental bands due to a weakening of the shock caused by decreases in the velocity of the CME at the rear of the shock.

[67] An investigation of beam parameters along the shock front at the nose of the CME-driven shock reveals that for this simulation the electron temperatures are slightly higher north, as opposed to south, of the shock near the nose region. The heating of the northern plasma is due to previous magnetic reconnection, which dissipates magnetic energy and leads to plasma heating and bulk flow, between anti-parallel magnetic field lines of the body of the CME and the external distorted radial magnetic field of the Sun, which are pushed together as the CME moves out. This distortion is significant, leading to angles between magnetic field and the shock normal at the intersection point with the shock front of about 45° on average in the northern hemisphere and of about 35° in the southern hemisphere. Thus, the cutoff speeds for the reflected beam are slightly larger north than south of the nose of the shock. Despite θ_{bn} being $\leq 70^\circ$ here, the cutoff speeds are comparable with two times the electron thermal speed near the nose of the shock. Thus, radio emission is not entirely suppressed there, although it is quite weak. Since the shock normal turns away from the radial direction toward the flanks of the shock, the cutoff and beam speeds of the electrons leaving the shock diminish in the same directions, and the crescent-like radio source fades away. The maximum of the radio source is situated slightly above the ecliptic plane due to the asymmetry in the magnetic field configuration about the nose of the shock.

[68] A more complete discussion of the radio emission arising from the CME-driven shock in this simulation, specifically including emission from the rippled flanks of the shock is presented in a companion paper (*Schmidt and Cairns*, manuscript in preparation, 2012). The limitations of the basic radio theory and its application to type II bursts are discussed elsewhere [*Cairns*, 2011].

[69] In conclusion, a fully analytic theoretical model for type II bursts now exists in a form suitable for combining with (or bolting onto) MHD or other shock simulations. This includes the electron reflection and acceleration at the shock, formation and plateauing of electron beams, quasilinear and SGT growth of Langmuir waves, and production of f_p and $2f_p$ radiation by standard nonlinear processes in macroscopic foreshock regions upstream of the shock. The theory is ready for extension to fully 3D source regions and detailed

application to type II bursts. It is suitable for bolting onto MHD and other simulations of shocks in applications to other space and astrophysical radio emissions associated with shocks.

Appendix A: Calculation of the Reflection Efficiency

[70] In this appendix we calculate the integral in the numerator of the reflection efficiency (3) for kappa electron velocity distributions explicitly. We obtain

$$\int_{v_c}^c 2\pi v_{\perp} f_{\kappa}(v_{\parallel}, v_{\perp}) dv_{\perp} \quad (\text{A1})$$

$$= \frac{\Gamma(\kappa+1)}{\Gamma(\kappa-\frac{1}{2})} \pi^{-1/2} v_e^{-3} \int_{v_c}^c \left(1 + \frac{v_{\parallel}^2 + v_{\perp}^2}{v_e^2}\right)^{-(\kappa+1)} d(v_{\perp}^2) \quad (\text{A2})$$

$$= \frac{\Gamma(\kappa+1)}{\Gamma(\kappa-\frac{1}{2})} \pi^{-1/2} v_e^{-1} \int_{v_c}^c \left(1 + \frac{v_{\parallel}^2 + v_{\perp}^2}{v_e^2}\right)^{-(\kappa+1)} \times d\left(1 + \frac{v_{\parallel}^2 + v_{\perp}^2}{v_e^2}\right) \quad (\text{A3})$$

$$= \frac{\Gamma(\kappa+1)}{\Gamma(\kappa-\frac{1}{2})} \pi^{-1/2} \frac{v_e^{-1}}{\kappa} \int_c^{v_c} d\left(\left(1 + \frac{v_{\parallel}^2 + v_{\perp}^2}{v_e^2}\right)^{-\kappa}\right) \quad (\text{A4})$$

$$= \frac{\Gamma(\kappa+1)}{\Gamma(\kappa-\frac{1}{2})} \pi^{-1/2} \frac{v_e^{-1}}{\kappa} \left[\left(1 + \frac{v_{\parallel}^2 + v_{lc}^2}{v_e^2}\right)^{-\kappa} - \left(1 + \frac{v_{\parallel}^2 + c^2}{v_e^2}\right)^{-\kappa} \right] \quad (\text{A5})$$

$$\approx \frac{\Gamma(\kappa+1)}{\Gamma(\kappa-\frac{1}{2})} \pi^{-1/2} \frac{v_e^{-1}}{\kappa} \left(1 + \frac{v_{\parallel}^2 + v_{lc}^2}{v_e^2}\right)^{-\kappa}, \quad (\text{A6})$$

since c/v_e is a very large number and the second term in the squared brackets in (A5) can thus be neglected. The denominator of the reflection efficiency (3) for kappa electron velocity distributions can be found with an equivalent calculation, where we replace v_{lc} with zero:

$$\int_0^c 2\pi v_{\perp} f_{\kappa}(v_{\parallel}, v_{\perp}) dv_{\perp} \approx \frac{\Gamma(\kappa+1)}{\Gamma(\kappa-\frac{1}{2})} \pi^{-1/2} \frac{v_e^{-1}}{\kappa} \left(1 + \frac{v_{\parallel}^2}{v_e^2}\right)^{-\kappa}. \quad (\text{A7})$$

Appendix B: Determination of Boundaries of the Quasilinear Plateau

[71] From Figure 5, using the trapezoidal rule we have

$$B \approx \frac{1}{2} [F_i(a) - F_i(v_c)](v_c - a), \quad (\text{B1})$$

$$A \approx \frac{1}{2} [F_i(v_c) + F_r(v_c) - F_i(b) - F_r(b)](b - v_c) \quad (\text{B2})$$

for the area B below the plateau and above the background electron velocity distribution $F_i(v_{\parallel})$ and for the area A below

the total velocity distribution $F_i(v_{\parallel}) + F_r(v_{\parallel})$ and above the plateau. Using a Taylor expansion around v_c for the distribution functions $F_i(v_{\parallel})$ and $F_r(v_{\parallel})$ yields

$$F_i(a) - F_i(v_c) \approx (-1)F_i'(v_c)(v_c - a), \quad (\text{B3})$$

$$F_i(v_c) + F_r(v_c) - F_i(b) - F_r(b) \approx [(-1)F_i'(v_c) + (-1)F_r'(v_c)] \cdot (b - v_c). \quad (\text{B4})$$

Note that both the trapezoidal rule and a first order Taylor expansion become more precise the larger v_c is, since both functions $F_i(v_{\parallel})$ and $F_r(v_{\parallel})$ have a more uniform slope the further we move into the high velocity tail. Thus,

$$B \approx \frac{1}{2} (-1)F_i'(v_c)(v_c - a)^2, \quad (\text{B5})$$

$$A \approx \frac{1}{2} [(-1)F_i'(v_c) + (-1)F_r'(v_c)](b - v_c)^2, \quad (\text{B6})$$

and the condition $B = A$ implies

$$D(b - v_c)^2 = C(v_c - a)^2, \quad (\text{B7})$$

$$\text{where } D = [(-1)F_i'(v_c) + (-1)F_r'(v_c)], \quad (\text{B8})$$

$$C = (-1)F_i'(v_c). \quad (\text{B9})$$

On the other hand, we have

$$F_i(a) \approx F_i(v_c) + F_i'(v_c)(a - v_c), \quad (\text{B10})$$

$$F_i(b) + F_r(b) \approx F_i(v_c) + F_r(v_c) + [F_i'(v_c) + F_r'(v_c)](b - v_c) \quad (\text{B11})$$

for the left and right boundary of the plateau. Since $F_i(a) = F_i(b) + F_r(b)$ on the plateau, then

$$\beta - \alpha(v_c - a) = (b - v_c), \quad (\text{B12})$$

$$\beta = \frac{F_r(v_c)}{[(-1)F_i'(v_c) + (-1)F_r'(v_c)]}, \quad (\text{B13})$$

$$\alpha = \frac{(-1)F_i'(v_c)}{[(-1)F_i'(v_c) + (-1)F_r'(v_c)]}. \quad (\text{B14})$$

If we substitute $(b - v_c)$ from equation (B12) into equation (B7), we obtain a quadratic equation for $(v_c - a)$ alone, which has the solutions

$$a = v_c - \frac{\alpha\beta D}{\alpha^2 D - C} \pm \sqrt{\left[\frac{\alpha\beta D}{\alpha^2 D - C}\right]^2 - \frac{\beta^2 D}{\alpha^2 D - C}}. \quad (\text{B15})$$

Resubstitution of constants (B8), (B9), (B13), and (B14) yields

$$a = v_c - \frac{F_r(v_c)}{(-1)F_r'(v_c)} \left\{ \sqrt{1 + \frac{(-1)F_i'(v_c)}{(-1)F_i'(v_c)}} - 1 \right\} \quad (\text{B16})$$

where we dropped the positive sign, since we require $a < v_c$. Substituting equation (B16) into equation (B12) then yields

$$b = v_c + \frac{F_r(v_c)}{[(-1)F'_i(v_c) + (-1)F'_r(v_c)]} \times \left[1 - \frac{(-1)F'_i(v_c)}{(-1)F'_r(v_c)} \left\{ \sqrt{1 + \frac{(-1)F'_r(v_c)}{(-1)F'_i(v_c)} - 1} \right\} \right]. \quad (\text{B17})$$

Taking $F_r(v_{||})$ and $F_i(v_{||})$ from equations (16) and (14), we find

$$a = v_c - \frac{v_e^2}{2\kappa v_c} \left(1 + \left(\frac{v_c}{v_e} \right)^2 + \frac{\frac{2}{m_e} e \Delta \Phi'}{v_e^2 (B_2/B_1 - 1)} \right) \times \left\{ \sqrt{1 + \left(\frac{1 + \left(\frac{v_c}{v_e} \right)^2}{1 + \left(\frac{v_c}{v_e} \right)^2 + \frac{\frac{2}{m_e} e \Delta \Phi'}{v_e^2 (B_2/B_1 - 1)}} \right)^{(\kappa+1)}} - 1 \right\}, \quad (\text{B18})$$

$$b = v_c + \frac{v_e^2}{2\kappa v_c} \frac{\left(1 + \left(\frac{v_c}{v_e} \right)^2 + \frac{\frac{2}{m_e} e \Delta \Phi'}{v_e^2 (B_2/B_1 - 1)} \right)^{(\kappa+1)}}{\left[1 + \left(\frac{1 + \left(\frac{v_c}{v_e} \right)^2 + \frac{\frac{2}{m_e} e \Delta \Phi'}{v_e^2 (B_2/B_1 - 1)}}{1 + \left(\frac{v_c}{v_e} \right)^2} \right)^{(\kappa+1)} \right]} \times \left[1 - \left(\frac{1 + \left(\frac{v_c}{v_e} \right)^2 + \frac{\frac{2}{m_e} e \Delta \Phi'}{v_e^2 (B_2/B_1 - 1)}}{1 + \left(\frac{v_c}{v_e} \right)^2} \right)^{(\kappa+1)} \right] \times \left\{ \sqrt{1 + \left(\frac{1 + \left(\frac{v_c}{v_e} \right)^2}{1 + \left(\frac{v_c}{v_e} \right)^2 + \frac{\frac{2}{m_e} e \Delta \Phi'}{v_e^2 (B_2/B_1 - 1)}} \right)^{(\kappa+1)}} - 1 \right\}. \quad (\text{B19})$$

Appendix C: Field Lines in the x - z Plane

[72] In the $r - \theta$ plane, a trajectory is given parametrically by a pair of functions $(r(\lambda), \theta(\lambda))$, where λ is a scalar parameter. Such a trajectory is a magnetic field line if its tangent is proportional to the magnetic field. Hence,

$$\frac{dr(\lambda)}{d\lambda} = r B_r \sin \theta, \quad (\text{C1})$$

$$r \frac{d\theta(\lambda)}{d\lambda} = r B_\theta \sin \theta, \quad (\text{C2})$$

defines a magnetic field line, where we have chosen $r \sin \theta$ as proportionality factor. Note that $r d\theta$ is the line-element in the θ -direction. In spherical coordinates it is

$$B_r = (\nabla \times \mathbf{A})_r = \frac{1}{r \sin \theta} \frac{\partial}{\partial \theta} (\sin \theta A_\phi) - \frac{1}{r \sin \theta} \frac{\partial A_\phi}{\partial \phi}, \quad (\text{C3})$$

$$= \frac{1}{r \sin \theta} \frac{\partial}{\partial \theta} (\sin \theta A_\phi), \quad (\text{C4})$$

$$B_\theta = (\nabla \times \mathbf{A})_\theta = \frac{1}{r \sin \theta} \frac{\partial A_r}{\partial \phi} - \frac{1}{r} \frac{\partial}{\partial r} (r A_\phi), \quad (\text{C5})$$

$$= -\frac{1}{r} \frac{\partial}{\partial r} (r A_\phi), \quad (\text{C6})$$

if there is no ϕ -dependence of the fields. This yields

$$\frac{dr(\lambda)}{d\lambda} = \frac{1}{r} \frac{\partial}{\partial \theta} (r \sin \theta A_\phi), \quad (\text{C7})$$

$$\frac{d\theta(\lambda)}{d\lambda} = -\frac{1}{r} \frac{\partial}{\partial r} (r \sin \theta A_\phi). \quad (\text{C8})$$

With this result we obtain

$$\frac{d}{d\lambda} (r \sin \theta A_\phi) = \frac{dr}{d\lambda} \frac{\partial}{\partial r} (r \sin \theta A_\phi) + \frac{d\theta}{d\lambda} \frac{\partial}{\partial \theta} (r \sin \theta A_\phi), \quad (\text{C9})$$

$$= \frac{1}{r} \frac{\partial}{\partial \theta} (r \sin \theta A_\phi) \frac{\partial}{\partial r} (r \sin \theta A_\phi) - \frac{1}{r} \frac{\partial}{\partial r} (r \sin \theta A_\phi) \frac{\partial}{\partial \theta} (r \sin \theta A_\phi), \quad (\text{C10})$$

$$= 0, \quad (\text{C11})$$

along one of such field lines. (C11) has the solution

$$r A_\phi \sin \theta = \text{constant}, \quad (\text{C12})$$

where a specific value of the constant is a label for a specific field line.

[73] **Acknowledgments.** Constructive comments from P. A. Robinson, V. L. Lobzin, and B. Li and support from the Australian Research Council are gratefully acknowledged.

[74] Philippa Browning thanks Bojan Vrsnak and another reviewer for their assistance in evaluating this paper.

References

- Aschwanden, M. (2004), *Physics of the Solar Corona*, Springer, New York.
- Aschwanden, M. J., S. J. Newmark, J.-P. Delaboudinière, W. M. Neupert, J. A. Klimchuk, G. A. Gary, F. Portier-Fozzani, and A. Zucker (1999), Three-dimensional stereoscopic analysis of solar active region loops. I. SOHO/EIT observations and temperatures of $(1.0-1.5) \times 10^6$ K, *Astrophys. J.*, 515, 842–867, doi:10.1086/307036.
- Bale, S. D., M. J. Reiner, J. L. Bougeret, M. L. Kaiser, S. Krucker, D. E. Larson, and R. P. Lin (1999), The source region of an interplanetary type II radio burst, *Geophys. Res. Lett.*, 26, 1573–1576.
- Benz, A. O., and T. Golla (1988), Radio emission of coronal shock waves, *Astron. Astrophys.*, 202, 267–274.
- Bougeret, J.-L., et al. (1995), Waves: The radio and plasma wave investigation on the Wind spacecraft, *Space Sci. Rev.*, 71, 231–263.
- Brueckner, G. E., et al. (1995), The Large Angle Spectroscopic Coronagraph (LASCO), *Sol. Phys.*, 162, 357–402.
- Burgess, D., C. C. Harvey, J.-L. Steinberg, and C. Lacombe (1987), Simultaneous observation of fundamental and second harmonic radio emission from the terrestrial foreshock, *Nature*, 330, 732–735.
- Cairns, I. H. (1986a), The source of free energy for type II solar radio bursts, *Publ. Astron. Soc. Aust.*, 6, 444–446.
- Cairns, I. H. (1986b), New waves at multiples of the plasma frequency upstream of the Earth's bow shock, *J. Geophys. Res.*, 91, 2975–2988.
- Cairns, I. H. (1987a), The electron distribution function upstream from the Earth's bow shock, *J. Geophys. Res.*, 92, 2315–2327.
- Cairns, I. H. (1987b), A theory for the Langmuir waves in the electron foreshock, *J. Geophys. Res.*, 92, 2329–2342.
- Cairns, I. H. (2011), Coherent radio emissions associated with solar system shocks, in *The Sun, the Solar Wind, and the Heliosphere*, edited by M. P. Miralles and J. Almeida, pp. 267–338, Springer, New York.
- Cairns, I. H., and S. F. Fung (1988), Growth of electron plasma waves above and below f_p in the electron foreshock, *J. Geophys. Res.*, 93, 7307–7317.
- Cairns, I. H., and S. A. Knock (2006), Predictions for dynamic spectra and source regions of type II radio bursts in the inhomogeneous corona and solar wind, in *Planetary Radio Emissions VI*, edited by H. O. Rucker, W. S. Kurth, and G. Mann, pp. 419–430, Verlag Ost. Akad., Wissenschaften, Vienna.
- Cairns, I. H., and D. B. Melrose (1985), A theory for the $2f_p$ radiation upstream of the Earth's bow shock, *J. Geophys. Res.*, 90, 6637–6640.

- Cairns, I. H., and P. A. Robinson (1997), First test of stochastic growth theory for the Langmuir waves in Earth's foreshock, *Geophys. Res. Lett.*, *24*, 369–372.
- Cairns, I. H., and P. A. Robinson (1999), Strong evidence for stochastic growth of Langmuir-like waves in Earth's foreshock, *Phys. Rev. Lett.*, *82*, 3066–3069.
- Cairns, I. H., P. A. Robinson, and R. R. Anderson (2000), Thermal and driven stochastic growth of Langmuir waves in the solar wind and Earth's foreshock, *Geophys. Res. Lett.*, *27*, 61–64.
- Cairns, I. H., S. A. Knock, P. A. Robinson, and Z. Kuncic (2003), Type II solar radio bursts: Theory and space weather implications, *Space Sci. Rev.*, *107*, 27–34.
- Cane, H. V., and R. G. Stone (1984), Type II solar radio bursts, interplanetary shocks, and energetic particle events, *Astrophys. J.*, *282*, 339–344.
- Cane, H. V., R. G. Stone, J. Fainberg, R. T. Stewart, J. L. Steinberg, and S. Hoang (1981), Radio evidence for shock acceleration of electrons in the solar corona, *Geophys. Res. Lett.*, *8*, 1285–1288.
- Cane, H. V., N. R. Sheeley, and R. A. Howard (1987), Energetic interplanetary shocks, radio emission, and coronal mass ejections, *J. Geophys. Res.*, *92*, 9869–9874.
- Cargill, P. J., J. M. Schmidt, D. S. Spicer, and S. T. Zalesak (2000), Magnetic structure of overexpanding coronal mass ejections: Numerical models, *J. Geophys. Res.*, *105*, 7509–7520.
- Cremades, H., and V. Bothmer (2004), On the three-dimensional configuration of coronal mass ejections, *Astron. Astrophys.*, *422*, 307–322.
- Crooker, N., J. A. Joselyn, and J. Feynman (1997), *Coronal Mass Ejections*, *Geophys. Monogr. Ser.*, vol. 99, edited by N. Crooker, J. A. Joselyn, and J. Feynman, 299 pp., AGU, Washington, D. C.
- DeVore, C. R. (1991), Flux-corrected transport techniques for multidimensional compressible MHD, *J. Comput. Phys.*, *92*, 142–160.
- Dulk, G. A., Y. Leblanc, P. A. Robinson, J.-L. Bougeret, and R. P. Lin (1998), Electron beams and radio waves of solar Type III bursts, *J. Geophys. Res.*, *103*, 17,223–17,233.
- Filbert, P. C., and P. J. Kellogg (1979), Electrostatic noise at the plasma frequency beyond the Earth's bow shock, *J. Geophys. Res.*, *84*, 1369–1381.
- Fitzreiter, R. J., J. D. Scudder, and A. J. Klimas (1990), Three-dimensional analytical model for the spatial variation of the foreshock electron distribution function: Systematics and comparisons with ISEE observations, *J. Geophys. Res.*, *95*, 4155–4173.
- Florens, M. S. L., I. H. Cairns, S. A. Knock, and P. A. Robinson (2007), Data-driven solar wind model and prediction of type II bursts, *Geophys. Res. Lett.*, *34*, L04104, doi:10.1029/2006GL028522.
- Forbes, T. G., et al. (2006), CME theory and models, *Space Sci. Rev.*, *123*, 251–302, doi:10.1007/s11214-006-9019-8.
- Goodrich, C. C., and J. D. Scudder (1984), The adiabatic energy change of plasma electrons and the frame dependence of the cross-shock potential at collisionless magnetosonic shock waves, *J. Geophys. Res.*, *89*, 6654–6662.
- Gopalswamy, N. (2006), Coronal mass ejections of solar cycle 23, *J. Air Waste Manage. Assoc.*, *27*, 243–254.
- Gopalswamy, N., A. Lara, R. P. Lepping, M. L. Kaiser, D. Berdichevsky, and O. C. St. Cyr (2000), Interplanetary acceleration of coronal mass ejections, *Geophys. Res. Lett.*, *27*, 145–148.
- Gopalswamy, N., E. Aguilar-Rodriguez, S. Yashiro, S. Nunes, M. L. Kaiser, and R. A. Howard (2005), Type II radio bursts and energetic solar eruptions, *J. Geophys. Res.*, *110*, A12S07, doi:10.1029/2005JA011158.
- Gosling, J. T., P. Riley, D. J. McComas, and V. J. Pizzo (1998), Overexpanding coronal mass ejections at high heliographic latitudes: Observations and simulations, *J. Geophys. Res.*, *103*, 1941–1954.
- Hillan, D., I. H. Cairns, and P. A. Robinson (2011), Type II solar radio bursts: Extraction of shock parameters and detailed comparison of theory with observations, *J. Geophys. Res.*, *117*, A03104, doi:10.1029/2011JA016754.
- Hoang, S., J. Fainberg, J.-L. Steinberg, R. G. Stone, and R. H. Zwickl (1981), The $2f_p$ circumterrestrial radio emission as seen from ISEE 3, *J. Geophys. Res.*, *86*, 4531–4536.
- Holman, G. D., and M. E. Pesses (1983), Solar type II radio emission and the shock drift acceleration of electrons, *Astrophys. J.*, *267*, 837–843.
- Howard, R. A., J. D. Moses, and A. Vourlidas (2008), Sun Earth Connection Coronal and Heliospheric Investigation (SECCHI), *Space Sci. Rev.*, *136*, 67–115.
- Hundhausen, A. J. (1999), Coronal mass ejections, in *The Many Faces of the Sun: A Summary of the Results From NASA's Solar Maximum Mission*, edited by K. T. Strong et al., pp. 143–230, Springer, New York.
- Hundhausen, A. J., C. B. Sawyer, L. L. House, R. M. E. Illing, and W. J. Wagner (1984), Coronal mass ejections observed during the Solar Maximum Mission: Latitude distribution and rate of occurrence, *J. Geophys. Res.*, *89*, 2639–2646.
- Kasaba, Y., H. Matsumoto, Y. Omura, R. R. Anderson, and T. Mukai (2000), Statistical studies of plasma waves and Backstreaming electrons in the terrestrial electron foreshock observed by Geotail, *J. Geophys. Res.*, *105*, 79–103.
- Klein, L. W., and L. F. Burlaga (1982), Interplanetary magnetic clouds at 1 AU, *J. Geophys. Res.*, *87*, 613–624.
- Knock, S. A., and I. H. Cairns (2005), Type II radio emission predictions: Sources of coronal and interplanetary spectral structure, *J. Geophys. Res.*, *110*, A01101, doi:10.1029/2004JA010452.
- Knock, S. A., I. H. Cairns, P. A. Robinson, and Z. Kuncic (2001), Theory of type II radio emission from the foreshock of an interplanetary shock, *J. Geophys. Res.*, *106*, 25,041–25,051.
- Knock, S. A., I. H. Cairns, P. A. Robinson, and Z. Kuncic (2003a), Theoretically predicted properties of type II radio emission from an interplanetary foreshock, *J. Geophys. Res.*, *108*(A3), 1126, doi:10.1029/2002JA009508.
- Knock, S. A., I. H. Cairns, and P. A. Robinson (2003b), Type II radio emission predictions: Multiple shock ripples and dynamic spectra, *J. Geophys. Res.*, *108*(A10), 1361, doi:10.1029/2003JA009960.
- Kuncic, Z., I. H. Cairns, and S. Knock (2002), Analytic model for the electrostatic potential jump across collisionless shocks, with applications to Earth's bow shock, *J. Geophys. Res.*, *107*(A8), 1218, doi:10.1029/2001JA000250.
- Lacombe, C., C. C. Harvey, S. Hoang, A. Mangeney, J. L. Steinberg, and D. Burgess (1988), ISEE observations of radiation at twice the solar wind plasma frequency, *Ann. Geophys.*, *6*, 113–128.
- Lemen, J. R., et al. (2011), The Atmospheric Imaging Assembly (AIA) on the Solar Dynamics Observatory (SDO), *Sol. Phys.*, *275*, 17–40.
- Lengyel-Frey, D., T. Golla, R. J. MacDowall, R. G. Stone, and J. L. Phillips (1997), Ulysses observations of wave activity at interplanetary shocks and implications for type II radio bursts, *J. Geophys. Res.*, *102*, 2611–2621.
- Leroy, M. M., and A. Mangeney (1984), A theory of energization of solar wind electrons by the Earth's bow shock, *Ann. Geophys.*, *2*, 449–456.
- Lobzin, V. V., I. H. Cairns, and P. A. Robinson (2008), Evidence for wind-like regions, acceleration of shocks in the deep corona, and relevance of $1/f$ dynamic spectra to coronal type II bursts, *Astrophys. J.*, *677*, L129–L132.
- Maia, D., M. Pick, A. Vourlidas, and R. Howard (2000), Development of coronal mass ejections: Radio shock signatures, *Astrophys. J.*, *528*, L49–L51.
- Maksimovic, M., V. Pierrard, and P. Riley (1997), Ulysses electron distributions fitted with Kappa functions, *Geophys. Res. Lett.*, *24*, 1151–1154.
- Mann, G., and A. Klassen (2005), Electron beams generated by shock waves in the solar corona, *Astron. Astrophys.*, *441*, 319–326.
- Melrose, D. B. (1985), *Instabilities in Space and Laboratory Plasmas*, Cambridge Univ. Press, New York.
- Mitchell, J. J., I. H. Cairns, and P. A. Robinson (2004), Theory for 2–3 kHz radiation from the outer heliosphere, *J. Geophys. Res.*, *109*, A06108, doi:10.1029/2003JA010117.
- Nelson, G. J., and D. B. Melrose (1985), Type II bursts, in *Solar Radiophysics: Studies of Emission From the Sun at Metre Wavelengths*, edited by D. J. McLean and N. R. Labrum, pp. 333–359, Cambridge Univ. Press, New York.
- Neugebauer, M., and J. Giacalone (2005), Multispacecraft observations of interplanetary shocks: Nonplanarity and energetic particles, *J. Geophys. Res.*, *110*, A12106, doi:10.1029/2005JA011380.
- Nindos, A., C. E. Alissandrakis, A. Hillaris, and P. Preka-Papadema (2011), On the relationship of shock waves to flares and coronal mass ejections, *Astron. Astrophys.*, *531*, 31–43.
- Onsager, T. G., R. H. Holzworth, H. C. Koons, O. H. Bauer, and D. A. Gurnett (1989), High-frequency electrostatic waves near Earth's bow shock, *J. Geophys. Res.*, *94*, 13,397–13,408.
- Potter, D. W. (1981), Acceleration of electrons by interplanetary shocks, *J. Geophys. Res.*, *86*, 11,111–11,116.
- Pulupa, M. P., S. D. Bale, and J. C. Kasper (2010), Langmuir waves upstream of interplanetary shocks: Dependence on shock and plasma parameters, *J. Geophys. Res.*, *115*, A04106, doi:10.1029/2009JA014680.
- Reiner, M. J. (2000), Interplanetary type II radio emissions associated with CMEs, in *Radio Astronomy at Long Wavelengths*, *Geophys. Monogr. Ser.*, vol. 119, edited by R. G. Stone et al., pp. 137–145, AGU, Washington, D. C.
- Reiner, M. J., and M. L. Kaiser (1999), High-frequency type II radio emissions associated with shocks driven by coronal mass ejections, *J. Geophys. Res.*, *104*, 16,979–16,991.
- Reiner, M. J., M. L. Kaiser, J. Fainberg, J. L. Bougeret, and R. G. Stone (1997), Remote radio tracking of interplanetary CMEs, in *The 31st ESLAB Symposium on Correlated Phenomena at the Sun, in the Heliosphere, and in Geospace*, pp. 183–188, Eur. Space Agency, Noordwijk, Netherlands.

- Reiner, M. J., M. L. Kaiser, J. Fainberg, and R. G. Stone (1998), A new method for studying remote type II radio emissions from coronal mass ejection-driven shocks, *J. Geophys. Res.*, *103*, 29,651–29,664.
- Robinson, P. A. (1992), Clumpy Langmuir waves in type III solar radio sources, *Sol. Phys.*, *139*, 147–163.
- Robinson, P. A., and A. O. Benz (2000), Bidirectional type III solar radio bursts, *Sol. Phys.*, *194*, 345–369.
- Robinson, P. A., and I. H. Cairns (1995), Maximum Langmuir fields in planetary foreshocks determined from the electrostatic decay threshold, *Geophys. Res. Lett.*, *22*, 2657–2660.
- Robinson, P. A., and I. H. Cairns (1998a), Fundamental and harmonic emission in type III solar radio bursts-I. Emission at a single location or frequency, *Sol. Phys.*, *181*, 363–394.
- Robinson, P. A., and I. H. Cairns (1998b), Fundamental and harmonic emission in type III solar radio bursts-II. Dominant modes and dynamic spectra, *Sol. Phys.*, *181*, 395–428.
- Robinson, P. A., A. J. Willes, and I. H. Cairns (1993a), Dynamics of Langmuir and ion-sound waves in type III solar radio sources, *Astrophys. J.*, *408*, 720–734.
- Robinson, P. A., I. H. Cairns, and D. A. Gurnett (1993b), Clumpy Langmuir waves in type III radio sources: Comparison of stochastic-growth theory with observations, *Astrophys. J.*, *407*, 790–800.
- Robinson, P. A., I. H. Cairns, and A. J. Willes (1994), Dynamics and efficiency of type III radio emission, *Astrophys. J.*, *422*, 870–882.
- Robinson, P. A., B. Li, and I. H. Cairns (2004), New regimes of stochastic wave growth, *Phys. Rev. Lett.*, *93*, 235003, doi:10.1103/PhysRevLett.93.235003.
- Robinson, P. A., B. Li, and I. H. Cairns (2006), New regimes of stochastic wave growth: Theory, simulation, and comparison with data, *Phys. Plasmas*, *13*, 112103, doi:10.1063/1.2363174.
- Röttgering, H., M. van Haarlem, and G. Miley (2005), LOFAR-A new low frequency radio telescope, in *Probing Galaxies Through Quasar Absorption Lines: Proceedings of the 199th Colloquium of the International Astronomical Union*, edited by P. Williams, C.-G. Shu, and B. Menard, pp. 381–386, Cambridge Univ. Press, New York, doi:10.1017/S1743921305002851.
- Salah, J. E., C. J. Lonsdale, D. Oberoi, R. J. Cappallo, and J. C. Kasper (2005), Space weather capabilities of low frequency radio arrays, *Proc. SPIE Soc. Opt. Eng.*, *5901*, 124–134, doi:10.1117/12.613448.
- Schmidt, J. M. (2000), Flux ropes embedded in a radial magnetic field: Analytic solutions for the external magnetic field, *Sol. Phys.*, *197*, 135–148.
- Schmidt, J. M., and P. J. Cargill (2001), Magnetic cloud evolution in a two-speed solar wind, *J. Geophys. Res.*, *106*, 8283–8290.
- Schmidt, J. M., and P. J. Cargill (2003), Magnetic reconnection between a magnetic cloud and the solar wind magnetic field, *J. Geophys. Res.*, *108*(A1), 1023, doi:10.1029/2002JA009325.
- Schmidt, J. M., and P. J. Cargill (2004), A numerical study of two interacting coronal mass ejections, *Ann. Geophys.*, *22*, 2245–2254.
- Schmidt, J. M., and N. Gopalswamy (2008), Synthetic radio maps of CME-driven shocks below 4 solar radii heliocentric distance, *J. Geophys. Res.*, *113*, A08104, doi:10.1029/2007JA013002.
- Sheeley, N. R., R. A. Howard, M. J. Koomen, D. J. Michels, R. Schwenn, K. H. Mühlhäuser, and H. Rosenbauer (1985), Coronal mass ejections and interplanetary shocks, *J. Geophys. Res.*, *90*, 163–175.
- Sonnerup, B. U. O. (1969), Acceleration of particles reflected at a shock front, *J. Geophys. Res.*, *74*, 1301–1304.
- St. Cyr, O. C., et al. (2000), Properties of coronal mass ejections: SOHO LASCO observations from January 1996 to June 1998, *J. Geophys. Res.*, *105*, 18,169–18,186.
- Street, A. G., L. Ball, and D. B. Melrose (1994), Shock drift acceleration and type II solar radio bursts, *Publ. Astron. Soc. Aust.*, *11*, 21–24.
- Temmer, M., B. Vršnak, T. Žic, and A. M. Veronig (2009), Analytic modeling of the Moreton wave kinematics, *Astrophys. J.*, *702*, 1343–1352.
- Toptyghin, I. N. (1980), Acceleration of particles by shocks in a cosmic plasma, *Space Sci. Rev.*, *26*, 157–213.
- Webb, G. M., W. I. Axford, and T. Terasawa (1983), On the drift mechanism for energetic charged particles at shocks, *Astrophys. J.*, *270*, 537–553.
- Wild, J. P., and S. F. Smerd (1972), Radio bursts from the solar corona, *Annu. Rev. Astron. Astrophys.*, *10*, 159–196.
- Wu, C. S. (1984), A fast Fermi process: Energetic electrons accelerated by a nearly perpendicular bow shock, *J. Geophys. Res.*, *89*, 8857–8862.
- Yuan, X., I. H. Cairns, and P. A. Robinson (2007), Simulation of energetic electron bursts upstream of reforming shocks, *Astrophys. J.*, *671*, 439–446.
- Yuan, X., I. H. Cairns, and P. A. Robinson (2008), Numerical simulation of electron distributions upstream and downstream of high Mach number quasi-perpendicular collisionless shocks, *J. Geophys. Res.*, *113*, A08109, doi:10.1029/2008JA013268.
- Zalesak, S. T. (1979), Fully multidimensional flux-corrected transport algorithms for fluids, *J. Comput. Phys.*, *31*, 335–362.

I. H. Cairns and J. M. Schmidt, School of Physics, Physics Road, Building A29, University of Sydney, Sydney, NSW 2006, Australia. (cairns@physics.usyd.edu.au; jschmidt@physics.usyd.edu.au)